

Article

Sensitivity of Simulated Conditions to Different Parameterization Choices Over Complex Terrain in Central Chile

Jorge Arévalo ¹, Julio C. Marín ^{1,2,*}, Mailiu Díaz ³, Graciela Raga ⁴, Diana Pozo ^{1,2}, Ana María Córdova ¹ and Darrel Baumgardner ⁵

¹ Departamento de Meteorología, Universidad de Valparaíso, Valparaíso 2340000, Chile; jab@meteo.uv.cl (J.A.); diana.pozo@uv.cl (D.P.); anamaria.cordova@uv.cl (A.M.C.)

² Centro Interdisciplinario de Estudios Atmosféricos y Astroestadística, Universidad de Valparaíso, Valparaíso 2340000, Chile

³ Facultad de Ingeniería, Universidad Andrés Bello, Santiago 7550196, Chile; mailiu.diaz@unab.cl

⁴ Instituto de Ciencias de la Atmósfera y Cambio Climático, Del. Coyoacán, Universidad Nacional Autónoma de México (UNAM), Mexico City 04510, Mexico; raga@unam.mx

⁵ Droplet Measurement Technologies LLC, 2400 Trade Centre Ave STE B, Longmont, CO 80503, USA; darrel@dropletmeasurement.com

* Correspondence: julio.marin@meteo.uv.cl

Abstract: This study evaluates the performance of fourteen high-resolution WRF runs with different combinations of parameterizations in simulating the atmospheric conditions over the complex terrain of central Chile during austral winter and spring. We focus on the validation of results for coastal, interior valleys, and mountainous areas independently, and also present an in-depth analysis of two synoptic-scale events that occurred during the study period: a frontal system and a cut-off low. The performance of the simulations decreases from the coast to higher altitudes, even though the differences are not very clear between the coast and interior valleys for 10 m wind speeds and precipitation. The simulated vertical profiles show a warmer and drier boundary layer and a cooler and moister free atmosphere than observed. The choice of the land-surface model has the largest positive impact on near-surface variables with the five-layer thermal diffusion scheme showing the smallest errors. Precipitation is more sensitive to the choice of cumulus parameterizations, with the simplified Arakawa–Schubert scheme generally providing the best performance for absolute errors. When examining the performance of the model simulating rain/no-rain events for different thresholds, also the cumulus parameterizations better represented the false alarm ratio (FAR) and the bias score (BS). However, the Morrison microphysics scheme resulted in the best critical success index (CSI), while the probability of detection (POD) was better in the simulation without analysis nudging. Overall, these results provide guidance to other researchers and help to identify the best WRF configuration for a specific research or operational goal.

Keywords: WRF sensitivity studies; central Chile; complex terrain; case studies



Citation: Arévalo, J.; Marín, J.C.; Díaz, M.; Raga, G.; Pozo, D.; Córdova, A.M.; Baumgardner, D. Sensitivity of Simulated Conditions to Different Parameterization Choices Over Complex Terrain in Central Chile. *Atmosphere* **2024**, *15*, 10. <https://doi.org/10.3390/atmos15010010>

Academic Editor: Petroula Louka

Received: 21 September 2023

Revised: 16 November 2023

Accepted: 24 November 2023

Published: 21 December 2023



Copyright: © 2023 by the authors. Licensee MDPI, Basel, Switzerland. This article is an open access article distributed under the terms and conditions of the Creative Commons Attribution (CC BY) license (<https://creativecommons.org/licenses/by/4.0/>).

1. Introduction

Central Chile, located between 30 and 36° S along the west coast of South America, is home to more than half of the Chilean population. The region comprises the Central Valley, a nearly flat depression where Santiago city (>7.5 million people) is located, bounded to the west by the Chilean coastal range and to the east by the Andes Cordillera, both extending in a north–south direction and parallel to each other. Other main coastal and interior cities are located on the western side of the Chilean coastal range.

The region is characterized by a mild Mediterranean climate [1,2], located between the dry and hot conditions of northern Chile and the humid and cold conditions of southern Chile. It is year-round under the influence of the permanent subtropical Southeast Pacific (SEP) anticyclone [3,4] with annual mean precipitation ranging between 350 and 400 mm,

which falls on only 25–27 days (Chilean Weather Service, <https://climatologia.meteochile.gob.cl/> (accessed on 15 July 2022)), mainly due to the passage of cold fronts in austral fall and winter months (May–September), and to a lesser extent by cut-off lows [5–8].

Warm and dry conditions aloft, due to synoptic-scale adiabatic compression associated with the SEP anticyclone, and cold and moist conditions in the marine boundary layer generate a thermal inversion, typically located below 1 km, that is usually capped by stratus clouds [9–12]. An offshore area of lower surface pressure flanked by the outskirts of the SEP anticyclone and the continent, known as a “coastal low”, is another important synoptic feature more frequently affecting the region during the austral winter and spring months [13].

Numerical weather forecasts have been constantly improving in the past decades [14] due to a number of factors such as increased computer capacity and observational coverage, better model numerics, model initial conditions, and a better representation of the physical mechanisms controlling atmospheric processes. The increase in computer power has allowed the simulation of atmospheric processes at finer resolutions, on the order of 1 km or less. However, despite these improvements, the performance of numerical weather forecasts over complex terrain is still a challenge since real topographic features cannot be accurately represented at typical model resolutions, and the representations of energy, mass, and momentum exchange between the atmosphere and the surface in model parameterizations are based on the assumption of horizontally homogeneous and flat surfaces [15].

Many studies have conducted sensitivity experiments to different model physical parameterizations in complex terrain around the world, focused on improving the representation of convective processes and precipitation, the near-surface wind field, high pollution, and extreme events, among others [16–24]. In South America, sensitivity studies with the Weather Research and Forecast (WRF) model along the Andes Cordillera have focused on testing different resolutions [25], and different microphysics [26–28], cumulus [22], land-surface model [29,30], and PBL parameterizations [31–33]. These studies, particularly those performed over central Chile, have analyzed a few case studies over only a few days, have employed horizontal resolutions ranging between 3 and 10 km, or their analysis has focused on a small area. Studies focusing on 1 km (or less) horizontal resolutions have not considered many sensitivity simulations, mainly due to the large computational requirements.

The present study evaluates a relatively larger number (14) of WRF model sensitivity experiments at 1 km horizontal resolution over a relatively large area ($2^\circ \times 2^\circ$) in central Chile, larger than those employed in previously cited studies. Furthermore, this study spans a period of 83 days during austral winter and spring. As mentioned above, the region is composed of different geographical features (coastal, relatively flat interior valleys, and mountain sites), whose near-surface conditions may show different temporal variability [34,35] and their representation in numerical forecasts may differ [36]. We aim to identify the physical parameterizations with the best performance or those with the largest limitations in simulating the atmospheric conditions over the entire region, as well as over the different sub-regions (coastal, interior valleys, or mountains). In addition, we quantify how the different sensitivity experiments represent two case studies that affected the region during the study period: a cold front and a cut-off low, which are associated with high winds, low temperatures, increased cloudiness, and precipitation. The results from this study can provide guidelines that can be used in future WRF model settings for operational and research activities over central Chile and other regions around the world with similar geographical features.

The paper is organized as follows: Section 2 describes the model sensitivity simulations, the observations used to assess their performance, and a description of the sub-regions analyzed; Section 3 evaluates the performance of simulations over coastal, interior valleys, and mountain sites during the whole period, and specifically during the occurrence of the

two case studies. Finally, a discussion of the results and the conclusions is provided in Section 4.

2. Data and Methods

2.1. WRF Model Sensitivity Experiments

We used the Advanced Research module of the Weather Research and Forecasting (WRF) model, version 3.6.1 [37]. A control (ctr) simulation was configured with four nested domains, as depicted in Figure 1a, with 27, 9, 3, and 1 km horizontal resolutions. Only the results from the smallest domain (domain 4, D4), with the highest resolution (1 km), are presented here. This domain includes the Santiago metropolitan area, several coastal and interior cities to the west-northwest, and part of the Andes Cordillera to the East. The simulation employed land-use data based on the Moderate Resolution Imaging Spectroradiometer (MODIS) at 30 arc seconds (approximately 0.9 km in horizontal resolution).

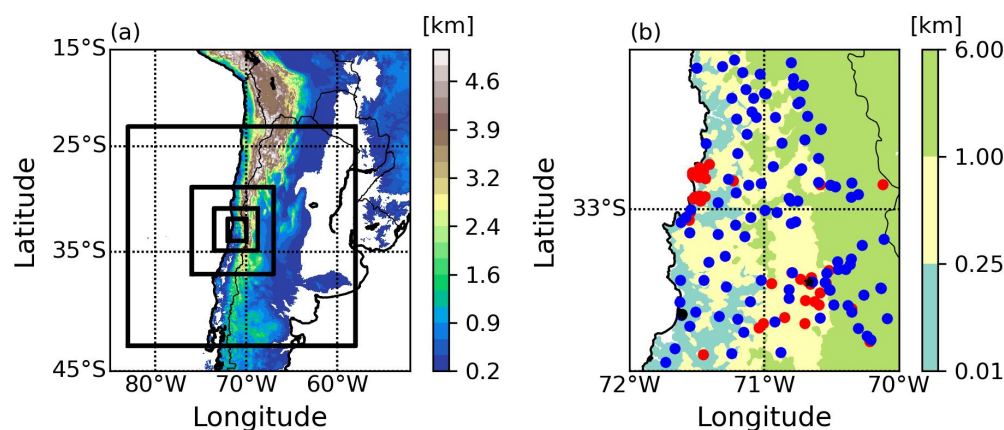


Figure 1. (a) The WRF 4-nested domain configuration and (b) the location of atmospheric weather stations (red circles), the rain gauges (blue circles), and the Santo Domingo radiosonde station (black circle) superimposed on domain D4. The black star shows the location of Santiago's center and the shaded colors represent the terrain altitude from D4, separated by the three ranges used to select coastal, interior valley, and mountainous locations in the study.

The ctr simulation included 60 vertical levels at variable resolution and with enhanced density near the surface and the tropopause. It was run for 83 days between 25 July and 15 October 2014 to simulate the atmospheric conditions during the Valparaiso Atmospheric Measurements of Pollution and Impact on the Regional Environment (VAMPIRE; [38,39]) and the Pollution Impact on Snow in the Cordillera-Experiments and Simulations (PISCES; [40]) field campaigns, two collaborative projects between different universities of Chile, Mexico, Brazil, and Spain. The Climate Forecast System version 2 (CFSv2, [41]) provided the initial and boundary conditions for the simulation every 6 h, and output fields were saved every 1 h. An analysis nudging [42–44] was implemented in the outer domain (D1) to provide better boundary conditions to the interior domains during the simulation period. Furthermore, we set a 2-way interaction, which allows the inner domains to also provide feedback to their parent domains.

The control simulation used the RRTMG [45] parameterization to calculate shortwave and longwave radiation. Convective processes in domains 1–3 were calculated with the Tiedtke scheme [46,47], while the WRF single-moment (WSM) 6-class scheme [48], which includes ice, snow, and graupel processes, was used for microphysics. The Mellor–Yamada Nakanishi and Niino Level 2.5 [49] was used for the planetary boundary layer (PBL), and the Noah Land Surface Model (LSM) [50] was used to parameterize the surface–atmosphere interaction in all domains. The Noah scheme forecasts the soil temperature and moisture and also provides fractional snow cover and frozen soil physics.

Thirteen more sensitivity simulations were run (for a total of 14) during the same 83 days to assess their performance in the central region of Chile. Eleven of them only

differed from the ctr simulation in one physical parameterization. Among the schemes tested on this study were the 5-layer (5L) thermal diffusion [51] and RUC [52] LSM schemes, the Yonsei University (YSU, [48]), the Mellor–Yamada–Janjic (MYJ, [53]), and the Grenier–Bretherton–McCaa (GBM, [54]) PBL schemes, the Kain–Fritsch (KF, [55]), new Grell [56,57]), and new simplified Arakawa–Schubert (SAS, [58] cumulus schemes, and the WRF single-moment 3-class (WSM3, [59]), the two-moment Morrison (Morr, [60]), and the WRF two-moment 6-class (WTM6, [61]) microphysics parameterizations. In addition, we performed two more simulations; one to test the impact of running the model without using analysis nudging, and another one using 1-way (the inner domains cannot provide feedback to their parent domains) instead of 2-way feedback in all domains. Table 1 describes the different simulations performed in this study and the labels we will use afterwards to refer to them in the text and figures. In summary, we will test a number of LSM, PBL, cumulus, and microphysics parameterizations. We are aware that other physical processes like radiation can have a notable influence on the representation of atmospheric conditions over the region. However, we did not test their influence in this study.

Table 1. Description of the configuration used in each of the 14 model runs. Changes with respect to the ctr simulation are highlighted in bold, depending on the land-surface model (LSM), microphysics (MP), cumulus, and planetary boundary layer (PBL) schemes employed, and the decision to use nudging or 1–2 feedback options.

No.	Sim	LSM	PBL	Cumulus	MP	Nudging	Feedback
1	ctr	Noah	MYNN2	Tiedtke	WSM6	Yes	2 way
2	cu1	Noah	MYNN2	KF	WSM6	Yes	2 way
3	cu5	Noah	MYNN2	Grell	WSM6	Yes	2 way
4	cu14	Noah	MYNN2	SAS	WSM6	Yes	2 way
5	lsm1	5L	MYNN2	Tiedtke	WSM6	Yes	2 way
6	lsm3	RUC	MYNN2	Tiedtke	WSM6	Yes	2 way
7	mp3	Noah	MYNN2	Tiedtke	WSM3	Yes	2 way
8	mp10	Noah	MYNN2	Tiedtke	Morr	Yes	2 way
9	mp16	Noah	MYNN2	Tiedtke	WTM6	Yes	2 way
10	no_fb	Noah	MYNN2	Tiedtke	WSM6	Yes	1 way
11	no_ng	Noah	MYNN2	Tiedtke	WSM6	No	2 way
12	pbl1	Noah	YSU	Tiedtke	WSM6	Yes	2 way
13	pbl2	Noah	MYJ	Tiedtke	WSM6	Yes	2 way
14	pbl12	Noah	GBM	Tiedtke	WSM6	Yes	2 way

We focused on how the 14 WRF simulations represented the near-surface and higher-level conditions, and the accumulated precipitation in the region during 83 days between 25 July and 15 October 2014. In addition to calculating mean statistical metrics for the whole domain of analysis, we also assessed the performance of the model over three different geographical settings present in central Chile: coastal, interior valley, and mountain sites. Stations were selected for each group based on their reported altitude or from the Google Maps information. Specifically, coastal sites are located below 250 m altitude, interior valleys are located between 250 and 1000 m, and mountain sites are those located above 1000 m in altitude (see the layering in Figure 1b). As a result, 8 coastal, 15 valley, and 3 mountain stations were selected to analyze the 2 m temperature and relative humidity (RH); 17 coastal, 12 valley, and 3 mountain stations were available to analyze the 10 m wind speed, and 27 coastal, 53 valley, and 24 mountain rain gauges were selected to analyze precipitation. Even though we only have three mountain stations for the analysis of temperature, RH, and wind speed, it is very important to assess the performance of simulations at those locations, where observations are scarce, to quantify their strengths and limitations and also to help us better understand the important processes associated with topography-enhanced precipitation, landslides, mountain flows, etc. We also analyzed in detail how the simulations represented two synoptic-scale events: a cold front and a cut-off low, which will be described in Section 3.3.

To highlight the complexity of the terrain in central Chile and the difficulty of simulating the atmospheric conditions over this surface, Figure 2 shows vertical cross-sections of the terrain height at the latitude of downtown Santiago (-33.45° S) from Google Earth (at ~ 0.44 km resolution) and from WRF domain 4 (~ 1 km horizontal resolution). On average, the nearest WRF grid points to the stations underestimate the station altitude by 11 m and 8.6 m in the coastal and interior valley regions, respectively. On the other hand, the nearest grid points overestimated the altitude of the mountain stations by 70 m on average.

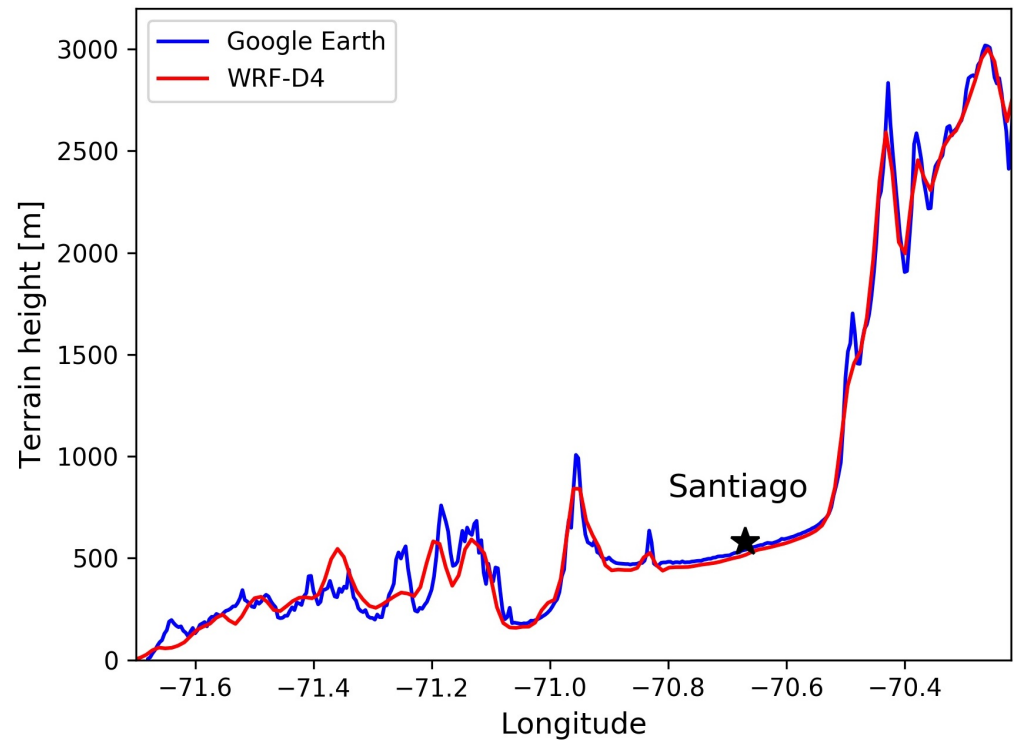


Figure 2. Height–longitude cross-section of terrain height from Google Earth (~ 0.44 km) and WRF domain 4 (1 km horizontal resolution) at the latitude -33.45° S. The black star represents the location of Santiago city.

During the period of study, four synoptic perturbations (3 cold fronts and 1 cut-off low) affected the region. Based on satellite images and the precipitation recorded at the stations, we selected all the days when the four synoptic systems affected central Chile, giving a total of 14 days, which we will label as perturbed (Table 2). As previously mentioned, the 14 WRF simulations were analyzed during 83 days between July and October 2014. We also focused on analyzing how the 14 different simulations represented the perturbed conditions (14 days affected by synoptic systems) compared to the other 14 unperturbed days (Table 2) that occurred during the whole study period. Among the perturbed days are the two study cases (a cold front and a cut-off low, highlighted in boldface in Table 2), which will be analyzed below. It is important to note that no rainfall was recorded during unperturbed days. Thus, we did not analyze the simulated precipitation during those days.

Table 2. Date and type of 14 perturbed days and the dates of 14 unperturbed days analyzed in this study.

Date	Event
5–6 August 2014	Cold front
22–24 August 2014	Cold front
29 August–5 September 2014	Cold front
13 September 2014	Cut-off low
9 August 2014	Unperturbed
12–15 August 2014	Unperturbed
18–20 August 2014	Unperturbed
26–27 August 2014	Unperturbed
11 September 2014	Unperturbed
15–17 September 2014	Unperturbed

2.2. Observations

We used the 10 m wind speed, 2 m temperature, and relative humidity (RH) observations from atmospheric weather stations (AWSs) that are part of the Chilean Weather Service (<https://www.meteochile.gob.cl/> (accessed on 1 July 2022)), the National System for Air Quality (<https://sinca.mma.gob.cl/> (accessed on 1 July 2022)) and the Agrometeorological (Agriculture Ministry, <http://agromet.inia.cl/> (accessed on 1 July 2022)) networks. We gathered 1-hourly data between 25 July and 14 October 2014 from a number of stations in central Chile, located between the coast and the Andes Cordillera. A total of 26 stations had reliable temperature and RH data for the period of study, whereas 32 stations were used in the analysis of wind speed.

Daily accumulated precipitation from 104 rain gauges was provided by the Center for Climate and Resilience Research (CR2, <http://www.cr2.cl/recursos-y-publicaciones/bases-de-datos/> (accessed on 15 July 2022)), whereas hourly precipitation data for the study cases were obtained at the Vismet site (<http://vismet.cr2.cl/> (accessed on 15 July 2022)), maintained by CR2. We also downloaded daily accumulated precipitation estimations from the Integrated Multi-Satellite Retrievals for the Global Precipitation Measurement (GPM) (IMERG) for the case studies.

Radiosondes in central Chile are launched every day at 0000 and 1200 UTC at Santo Domingo (code number 85586), the only radiosonde station located within the region. We used radiosonde data from Santo Domingo station at 1200 UTC for September and October 2014, since radiosondes were not launched on most days of August 2014 due to technical problems and those at 0000 UTC were not available. Figure 1b shows the location of the Santo Domingo radiosonde station, the AWSs, and the rain gauges used in this study, superimposed on WRF domain 4 (D4).

2.3. Model Evaluation

The performance of the WRF model was evaluated by examining the Pearson and Spearman correlations, the mean bias and the root mean squared error (RMSE) between simulations, and observations of 2 m temperature and RH, the 10 m wind speed, and precipitation. In addition to these metrics, for the case of precipitation, we also analyzed the probability of detection (POD), the false alarm ratio (FAR), the critical success index (CSI), and the bias score (BS) to examine the performance of the model in simulating rain/no-rain events for different thresholds. Each pair of observed and simulated rain events for a given precipitation threshold was then classified into four categories and a contingency table was created (Table 3), which allowed the calculation of the four metrics described below.

Table 3. Contingency table between the observed and simulated rainy events that defines the hits, misses, and false alarms for each specific threshold.

		Observed	
		Yes	No
Simulated	Yes	Hits	False alarms
	No	Misses	Correct non-events

The POD provides the proportion of rainfall events that are successfully simulated by the model and is calculated using the equation

$$POD = \frac{h}{h + m} \quad (1)$$

where “*h*” (hits) indicates that the event with daily precipitation greater than the selected threshold was both observed and simulated, and “*m*” (misses) indicates that the observed rainfall value was above the threshold but the simulated value was below the threshold. A POD value of 1 indicates that the event was perfectly simulated.

The FAR estimates the number of simulated rainy events when no rainy event was observed and it is calculated using Equation (2). The term “*fa*” (false alarms) indicates that the observed daily precipitation value is below the threshold and the simulated rainy event is above the selected threshold. A FAR value of zero corresponds to the best score.

$$FAR = \frac{fa}{fa + h} \quad (2)$$

The BS evaluates the tendency of the model to underestimate ($BS < 1$) or overestimate ($BS > 1$) the observed rainy events. The BS is calculated using Equation (3), representing a ratio between the frequency of simulated rainy events to the frequency of observed events. BS equals one if the number of simulated events is the same as the number of observed events.

$$BS = \frac{h + fa}{h + m} \quad (3)$$

The CSI is the fraction of observed rainfall that is correctly simulated by the model and is calculated using the equation

$$CSI = \frac{h}{h + fa + m} \quad (4)$$

3. Results

3.1. Overall Performance in Central Chile

Almost all of the simulations showed Pearson linear and Spearman’s rank correlations above 0.6, they all showed a root mean squared error (RMSE) below 23.5%, and similar variability as the observations in the forecast of 2 m RH (Figure 3a and Table 4). Two simulations were distinctively different from the rest: lsm3 (using the RUC LSM) and lsm1 (using the 5-layer thermal diffusion LSM). They showed the lowest RMSEs (21.6% and 18.0%, respectively) and bias (−4.7% and 8.5%, respectively) among the simulations (Table 4). However, lsm1 showed less variability on its forecasts than the observations and it was the only simulation that overestimated the observed 2 m RH. This may be related to the fact that among the three LSMs used in the sensitivity experiments, lsm1 is the only one that does not explicitly calculate the humidity at soil levels but uses climatological values to estimate it. On the other hand, pbl2 (with the MYJ PBL scheme) and cu14 (SAS cumulus parameterization) are the simulations that showed the worst performance (largest RMSE and bias) in representing the 2 m RH in the region during the study period.

Table 4. The RMSE, bias, and Spearman’s rank correlation coefficient (ρ) between each simulation and the observed 2 m RH and temperature, and the 10 m wind speed, averaged over the whole domain and the period of study. The simulations with the lowest value for RMSE, bias, and the highest rank correlation coefficient for each variable are shown in boldface.

Sim	RH			Temperature			Wind Speed		
	RMSE	Bias	ρ	RMSE	Bias	ρ	RMSE	Bias	ρ
ctr	22.4	−13.2	0.7	3.9	1.6	0.8	1.9	0.9	0.4
cu1	22.6	−13.2	0.7	3.9	1.6	0.8	1.9	0.8	0.4
cu5	21.8	−12.1	0.7	3.9	1.5	0.8	1.9	0.8	0.4
cu14	23.4	−14.3	0.7	4.0	1.7	0.8	1.9	0.8	0.4
lsm1	18.0	8.5	0.7	2.8	−0.2	0.9	1.8	0.6	0.4
lsm3	21.6	−4.7	0.6	3.7	1.1	0.8	1.6	0.4	0.4
mp3	22.2	−13.0	0.7	3.9	1.5	0.8	1.9	0.8	0.4
mp10	22.0	−13.1	0.7	3.8	1.5	0.8	1.9	0.8	0.4
mp16	22.2	−12.2	0.7	3.8	1.4	0.8	1.9	0.9	0.4
no_fb	22.2	−12.7	0.7	3.8	1.5	0.8	1.9	0.8	0.4
no_ng	22.7	−13.3	0.7	3.9	1.5	0.8	1.9	0.9	0.4
pbl1	22.8	−13.8	0.6	4.1	2.0	0.8	2.0	1.0	0.4
pbl2	23.3	−14.7	0.6	4.2	2.4	0.8	2.4	1.4	0.5
pbl12	22.7	−14.0	0.7	4.1	2.0	0.8	2.0	0.9	0.4

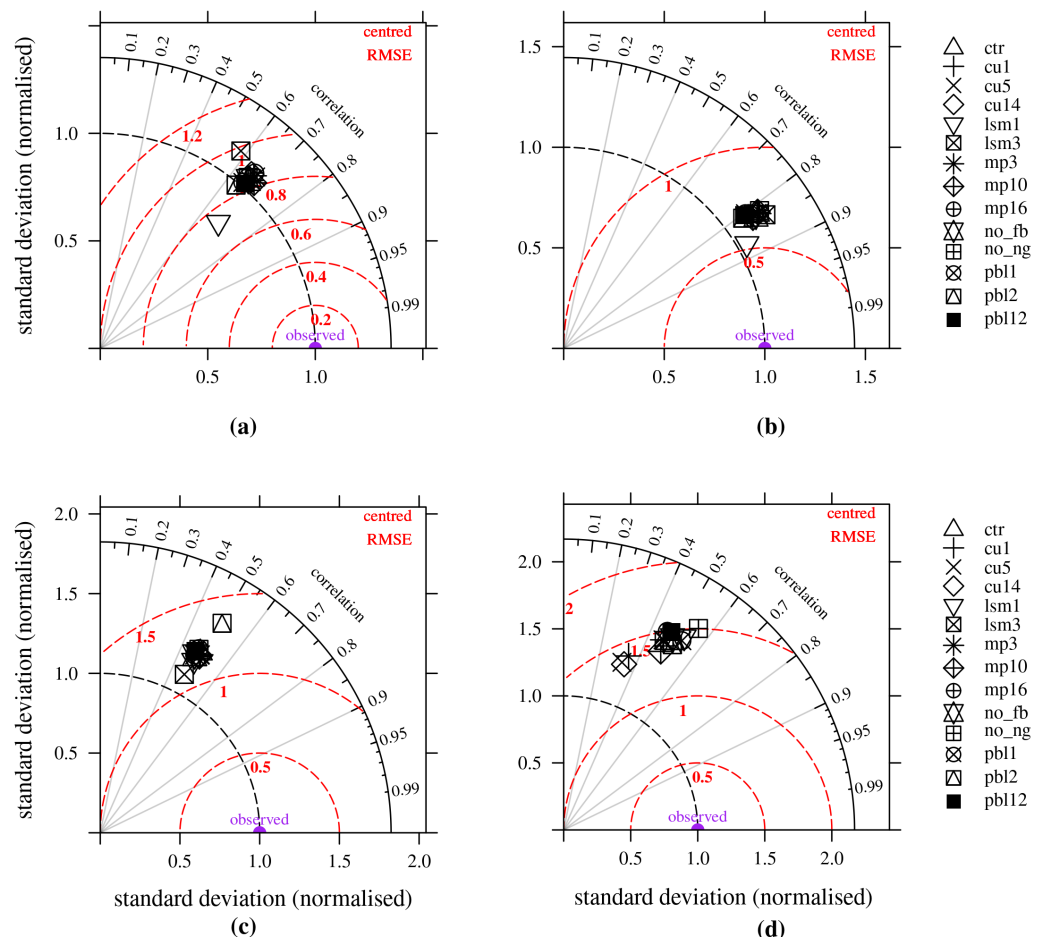


Figure 3. Taylor diagrams of (a) 2 m RH, (b) 2 m temperature, (c) 10 m wind speed, and (d) daily accumulated precipitation for all simulations averaged over the whole domain and period of study. Diagrams include the normalized standard deviation (nsdev) on the x- and y-axis, the Pearson correlation coefficient along the azimuth, and the centered RMSE difference (radially from nsdev reference value 1).

The 2 m temperature forecasts from almost all of the simulations show strong (>0.75) Pearson and Spearman correlations with observations in the region (Figure 3b and Table 4). All the simulations are placed at similar positions on the Taylor diagram, except lsm1, which shows the best agreement with the observations. It presents the largest correlations, the smallest RMSE and bias (Table 4), and its forecast temperature variability is closer to that observed (Figure 3b).

Figure 3c and Table 4 show moderate Pearson and Spearman correlation values (0.4–0.5) for 10 m wind speed forecasts in all simulations. Two simulations show the larger differences than the rest in the Taylor diagram. The pbl2 run (with the MYJ PBL parameterization) shows the largest RMSE (2.4 ms^{-1}) and bias (1.4 ms^{-1}) among the simulations over the whole period and the largest difference with the observed wind speed variability. In contrast, the lsm3 simulation shows the lowest RMSE (1.6 ms^{-1}) and bias (0.4 ms^{-1}), and the wind speed variability closest to the observations.

The Pearson and Spearman rank correlations for the accumulated precipitation forecasts in the region vary between 0.3 and 0.6 (Figure 3d and Table 5). The cu14 simulation (using the SAS cumulus scheme) shows the lowest RMSE and bias, and the closest variation to the observations among the simulations. On the other hand, the simulation with no analysis nudging (no_ng) shows the largest RMSE and bias, although it shows a slightly larger Spearman coefficient. Since cu14 and no_ng simulations show the best and worst agreements, respectively, with rain gauges over the domain and period of study, we will use both simulations in Section 3.3 to analyze the two case studies: a cold front and a cut-off low.

Table 5. The RMSE, bias, and Spearman’s rank correlation coefficient (ρ) for the daily accumulated precipitation ($>1 \text{ mm}$) between each simulation and observations, averaged over the whole domain and the period of study. The simulation with the lowest value of RMSE and bias, and the highest rank correlation coefficient, is shown in boldface.

Sim	Precipitation		
	RMSE	Bias	ρ
ctr	15.3	7.5	0.4
cu1	13.7	4.2	0.3
cu5	13.5	4.5	0.3
cu14	13.1	3.7	0.4
lsm1	15.2	7.4	0.4
lsm3	15.3	7.5	0.4
mp3	14.8	6.4	0.4
mp10	13.6	5.2	0.4
mp16	16.0	7.4	0.4
no_fb	15.0	7.3	0.4
no_ng	18.1	11.4	0.5
pbl1	15.4	8.3	0.4
pbl2	14.6	7.0	0.4
pbl12	15.9	7.7	0.4

All simulations represent the vertical distributions of temperature and the water vapor mixing ratio (qv) reasonably well compared to the Santo Domingo radiosondes, between 1 September and 15 October 2014 (Figure 4a,b). It is important to note that the largest differences between the simulations and observations for RH occurs near the surface, whereas those for temperature and wind speed occur near the surface but also around the tropopause level. However, we only focused here on the comparison between the surface and 700 hPa. Among all the simulations, cu14 and no_ng show the best and worst agreements with the observations, respectively, regarding the representation of the mean values and the variability shown over the period of analysis. Significant differences in temperature and qv between the simulations and observations occur in the PBL, below 900 hPa. Since the Santo Domingo sounding station is located just a few

hundred meters from the coast, these differences may be related to the fact that even though we are simulating the region at 1 km horizontal resolution, this may not be enough to accurately represent the coastline, the cold marine boundary layer, and the local land–sea circulations over the steep coastal terrain of the region. Thus, there are local cool, humid, and calm conditions frequently recorded by radiosondes in the first levels, which the model does not represent well. All the simulations show a boundary layer warmer and drier than observed, whereas, above it, they simulate a cooler and moister atmosphere. The wind speed is mainly overestimated in the layer 1000–700 hPa, except in the transition region between the boundary layer and the free atmosphere (Figure 4c). A mean low-level jet is observed at about 930 hPa, but it is simulated at a lower height. Overall, the largest errors in temperature and humidity occur in the boundary layer (below 850 hPa) and they decrease with height. However, wind speed forecasts show the opposite behavior.

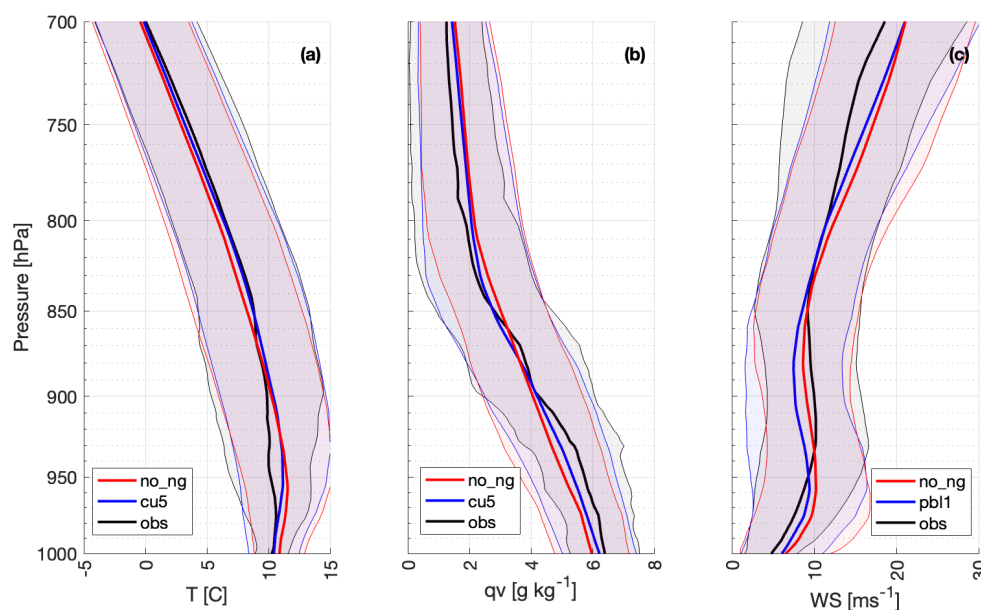


Figure 4. Mean (thick line) and standard deviation (thin line) profiles for the observed (black line) and simulated (a) temperature, (b) water vapor mixing ratio, and (c) wind speed. The blue and red lines on each panel show the simulations with the lowest and largest RMSE with the Santo Domingo radiosondes between 1 September and 14 October 2014. See the legend for details.

The performance of the simulations during the 14 perturbed days (those affected by synoptic perturbations) and 14 unperturbed days (Table 2) are similar in both groups. The same simulations show the best performance in both the perturbed and unperturbed days for each variable. All the simulations represent the 2 m temperature and RH better in the perturbed days, whereas the 10 m wind speed is better simulated on unperturbed days over the region (Figure 5a–c). In general, and similar to unperturbed days, all simulations overestimate the 2 m temperature and 10 m wind speed on perturbed days, whereas almost all of them underestimate the 2 m RH (Figure 5d–f).

Overall, the results indicate that changing the LSM parameterization causes the largest positive impact in representing the 2 m RH and temperature, and the 10 m wind speed forecasts in the region. Furthermore, the low sensitivity of such surface variables to nudging (Figure 5), for both perturbed and unperturbed days, supports the fact that the largest source of uncertainty comes from the physics parameterizations instead of the model dynamics. In contrast, precipitation shows a large sensitivity to the nudging option and to the cumulus parameterizations in the outer domains, therefore having a large dependence on both the dynamical and physical representations.

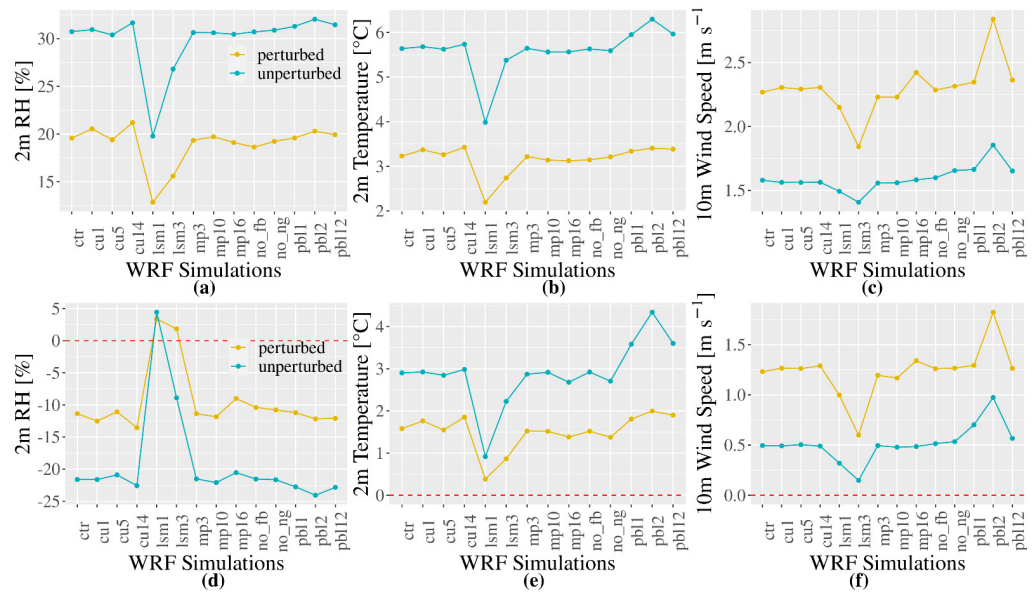


Figure 5. Mean RMSE for (a) 2 m RH, (b) 2 m temperature, and (c) 10 m wind speed for each simulation for perturbed and unperturbed days over the domain of study. (d–f) Same as (a–c), but for the mean bias.

3.2. Sub-Regional Analysis

In this section, we analyze the performance of the WRF model in representing the conditions of the three sub-regions: near the coast (<250 m), interior valleys (250–1000 m), and mountain sites (>1000 m).

In general, the performance of simulated 2 m temperature and RH, 10 m wind speed, and the accumulated precipitation decreases from the coast inland to high-altitude sites (Table 6). It is important to note that the RMSE of the simulated 10 m wind speed is a bit lower over the interior valleys of central Chile than over the coast, which may be related to it being more difficult to represent the local circulation over coastal sites with steep terrain than over higher-altitude but flatter terrain. The performance of the simulations changes at mountain sites compared to coastal and interior locations. The 2 m RH is overestimated, whereas the 2 m temperature and 10 m wind speed are underestimated at the high-altitude mountain sites. The opposite occurs over the coast and the interior valleys (Table 6). In the case of precipitation, simulations transition from underestimation near the coast to overestimation in the high-altitude sites (Table 6).

Table 6. The RMSE and bias for 2 m temperature (temp), 2 m RH, 10 m wind speed (Wsp), and the daily accumulated precipitation (values > 1 mm), averaged over all simulations, for each sub-region of central Chile.

Variable	RMSE			Bias		
	<250 m	250–1000 m	>1000 m	<250 m	250–1000 m	>1000 m
2 m RH (%)	19.1	23.2	24.1	−9.8	−14.8	9.1
2 m Temp (°C)	3.0	3.9	5.7	1.1	2.5	−3.4
10 m Wind Speed (ms ^{−1})	1.9	1.5	3.2	1.1	0.7	−0.4
Precipitation (mm)	13.4	13.6	14.3	−1.9	1.5	5.9

The lsm1 and lsm3 simulations show, in general, the best performance in simulating the 2 m temperature, 2 m RH, and the 10 m wind speed over coastal and interior valley locations (Figures 6 and 7). However, their performance representing these variables is not as good over mountain sites (Figures 6 and 7). Despite this, since many more stations are located at coastal and interior valleys, the results over these sub-regions largely affect

the metrics shown in Table 4. The performance of the simulations at high-altitude sites shows large variability, with different simulations showing the best results for each specific variable. Analyzing more high-altitude sites during a much larger period may help clarify which would be the best model configuration to use under these conditions.

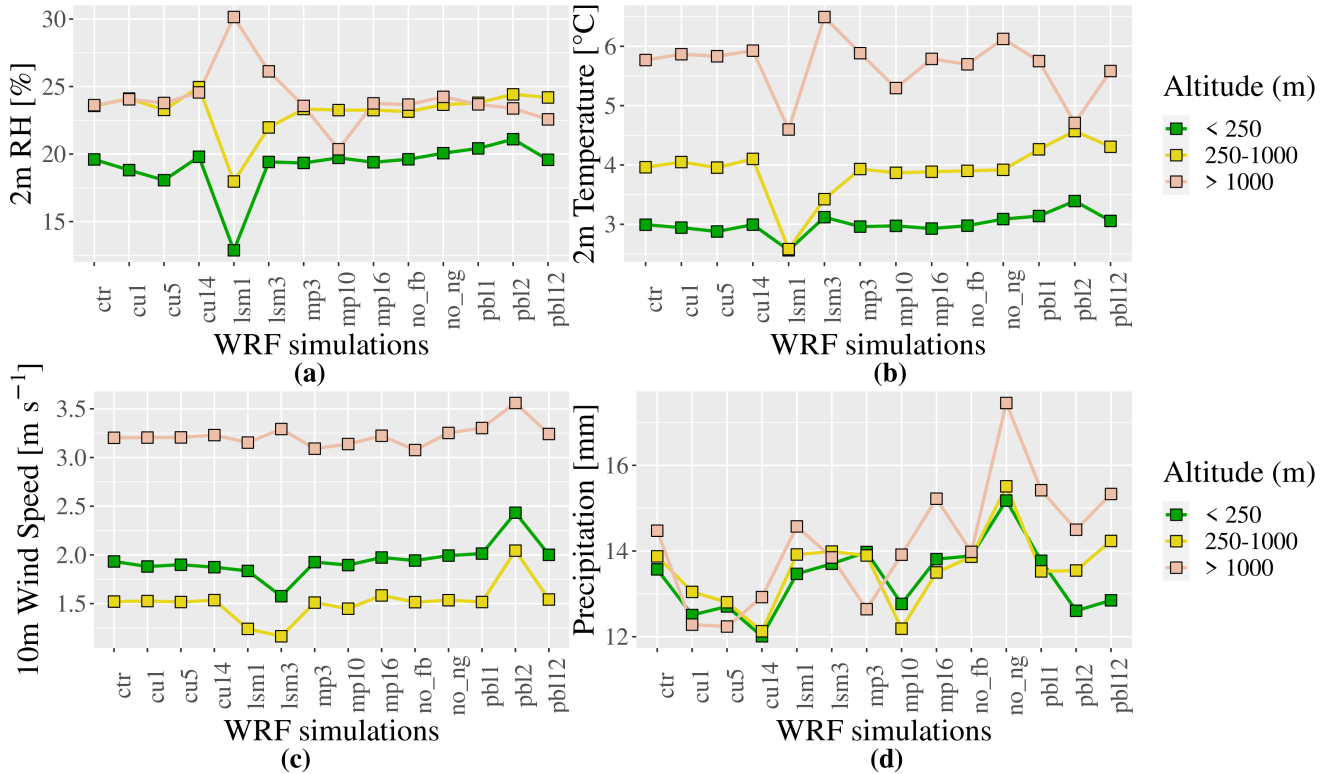


Figure 6. The RMSE between WRF simulations and observations for (a) 2 m RH, (b) 2 m temperature, (c) 10 m wind speed, and (d) accumulated precipitation over each sub-region.

The performance of daily accumulated precipitation is more variable among the simulations and sub-regions compared to the other variables. There is a clear indication that simulations changing the cumulus schemes consistently show the lowest errors. Simulations cu1, cu5, and cu14, with the Kain–Fritsch, Grell, and SAS cumulus schemes, respectively, reduce the RMSE (Figure 6d) in all sub-regions compared to the ctr simulation with the Tiedtke cumulus scheme. On the other hand, the *no_ng* simulation (without analysis nudging) largely increases the RMSE and bias in each sub-region compared to the other simulations. The benefit of analysis nudging to improve the representation of precipitation in climate simulations has been shown in other studies [43,62,63]. It is important to note that although it seems that precipitation forecasts are similar (based on the absolute errors) for coastal and interior valleys and in general unaffected by the parameterization scheme used for each sub-region, the results presented below show that precipitation forecasts change between sub-regions and are affected by the different parameterizations.

The analysis of the POD shows a different result. First of all, the proportion of rainfall events that are successfully simulated by the model increases from the coast to high-altitude sites (Figure 8). The *no_ng* simulation shows, in general, the best POD among the simulations, mainly for precipitation thresholds >8 mm/day (Figure 8a–c). The POD is larger for the smallest (<4 mm/day) and largest (>12 mm/day) rainfall thresholds but decreases for rainfall thresholds in between. In contrast, the simulations changing the cumulus (cu1, cu5, and cu14) and microphysics (mp3, mp10, mp16) parameterizations show the lowest POD in all sub-regions (Figure 8a–c).

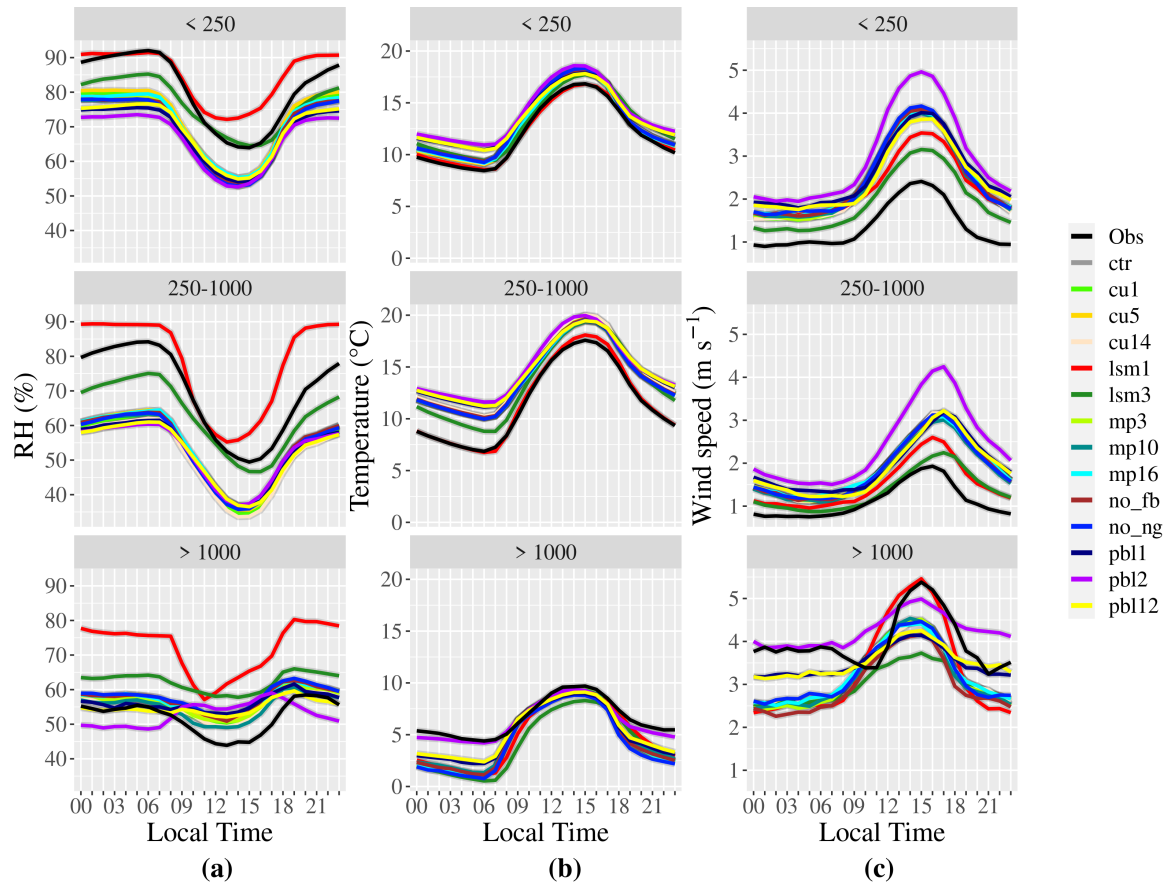


Figure 7. Diurnal variation of (a) 2 m RH, (b) 2 m temperature, and (c) 10 m wind speed, averaged over the period of study and for each sub-region.

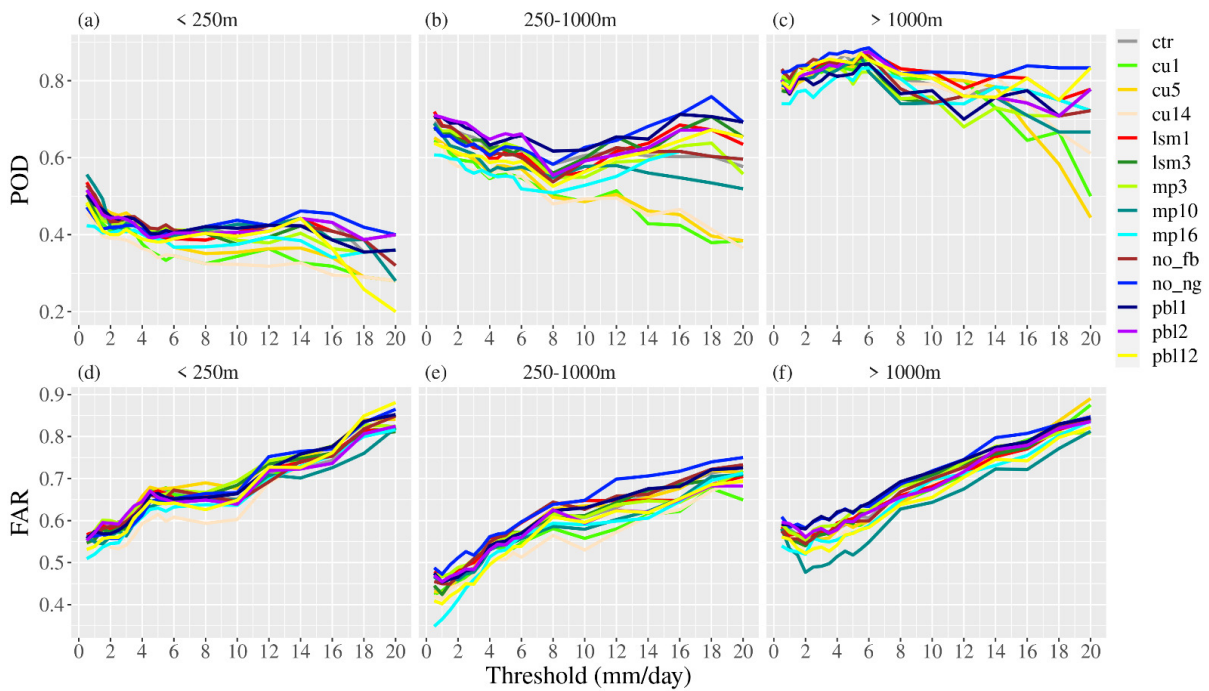


Figure 8. Probability of detection (POD) as a function of rainfall threshold for all WRF simulations and for (a) coastal, (b) interior valleys, and (c) mountain locations over the period of study. (d–f) Same as (a–c), but for the false alarm ratio (FAR).

The lowest number of rainy events simulated by the model that were not observed occurs in interior valleys (Figure 8d–f). The cu14 simulation shows in general the lowest FAR values among the simulations at coastal and interior valley locations, mainly for rainfall thresholds below 12 mm/day. However, other simulations changing the cumulus (cu1) and microphysics (mp10) schemes also show low FAR values in those sub-regions. At mountain sites, the lsm3 simulation shows the lowest FAR for all rainfall thresholds. On the other hand, the no_ng simulation shows in general the largest FAR values in all sub-regions.

All simulations overestimate the observed rainy events over the three sub-regions and for each specific threshold (Figure 9a–c). The overestimation in simulations linearly increases with rainfall thresholds in all sub-regions and the largest overestimation occurs over mountain sites (Figure 9c). The no_ng simulation shows the largest overestimation in each sub-region and for almost all rainfall thresholds. On the other hand, cu1, cu5, cu14, and mp16 show the lowest overestimation among the simulations in coastal and interior valley sites.

The fraction of observed rainfall thresholds correctly simulated by the model is larger for interior valleys and mountain sites (Figure 9d–f). This fraction is larger for low rainfall thresholds and decreases almost linearly with increasing rainfall thresholds for each sub-region. Despite the large variability in CSI values over the different sub-regions, it seems that mp10 shows, in general, the largest CSI values over the three sub-regions and for almost all rainfall thresholds.

It is important to note that the number of observations available for analysis decreases with altitude and, additionally, the number of high-precipitation events is reduced. Therefore, the results obtained for POD, FAR, BS, and CSI for mountain sites and large precipitation thresholds should be considered with caution since they may be largely dependent on the sample size.

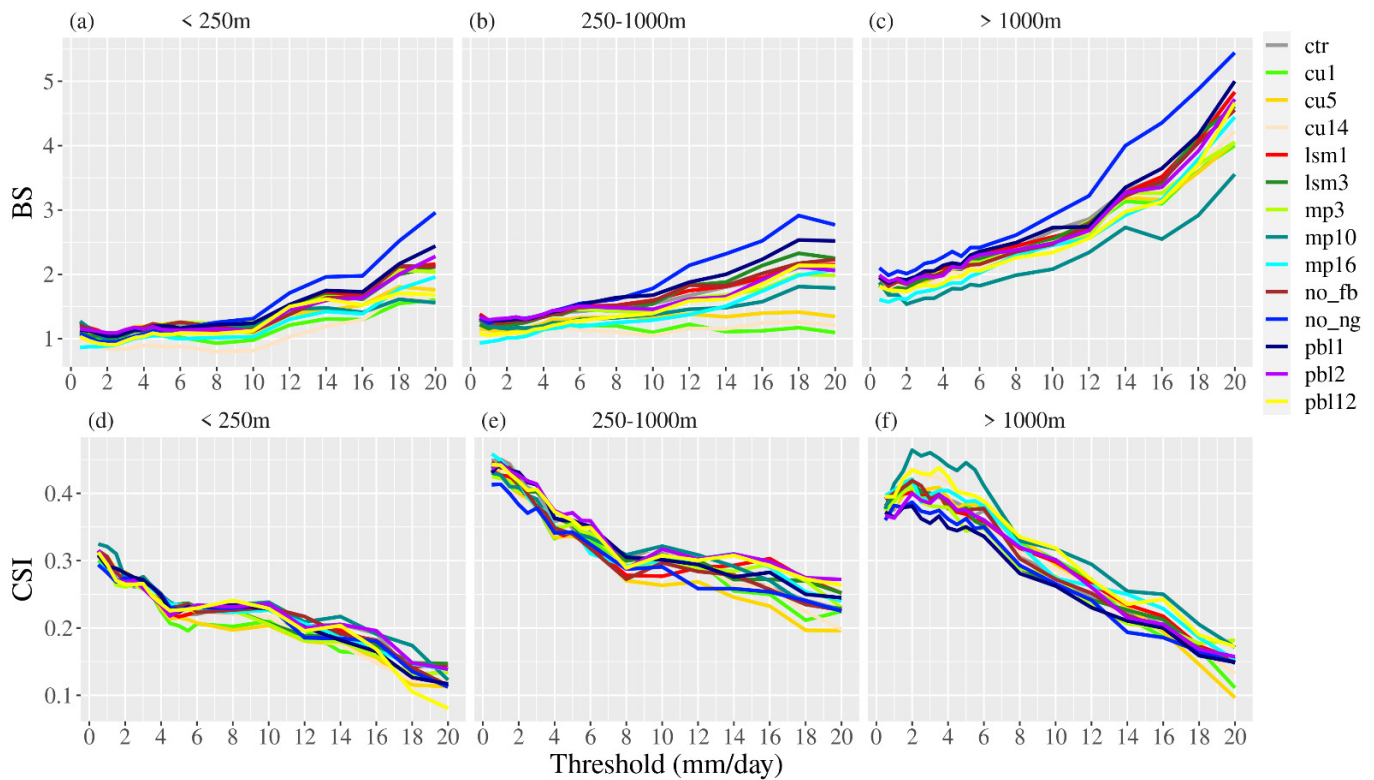


Figure 9. Bias score (BS) as a function of rainfall threshold for all WRF simulations and for (a) coastal, (b) interior valleys, and (c) mountain locations over the period of study. (d–f) Same as (a–c), but for the critical success index (CSI).

3.3. Case Studies

3.3.1. Frontal System: 6 August 2014

As was mentioned in the Introduction section, frontal systems affect central Chile mainly between May and September and are responsible for significantly increasing water resources in the region, via liquid and solid precipitation. A northwest–southeast aligned cold front approached the region from the southwest on 5 August 2014, which is indicated by low mean sea level pressure values to the south and a band of large precipitable water vapor (PWV) advected into the region (Figure 10a). A 500 hPa trough to the west (Figure 10a), as well as the subtropical jet located south of the study region (Figure 10b), also provided synoptic-scale favorable conditions for convective development and precipitation. The front reached the region on 6 August 2014 and gauge sensors located near the coast started recording precipitation late in the night that day and for 6–8 h. The precipitation was recorded in Santiago city and in the stations closer to the foothills of the Andes Cordillera from the early morning that day. The maximum daily accumulated precipitation ranged between 5 and 15 mm in the study region, with two stations located close to the Andes foothills reporting accumulated precipitation values larger than 20 mm.

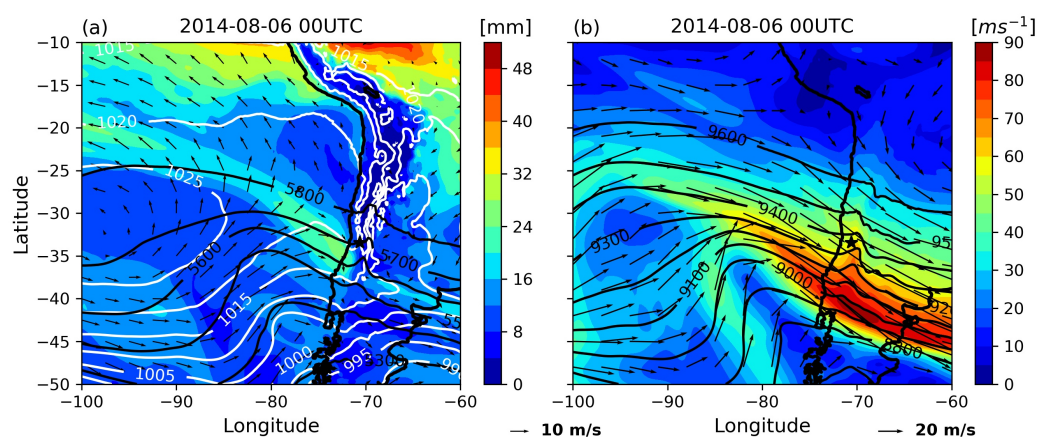


Figure 10. Horizontal distributions of (a) PWV (color shaded), MSLP (white contours), geopotential height at 500 hPa (black contours), and wind vectors at 10 m, and (b) wind speed (color shaded), geopotential height (black contours), and wind vectors at 300 hPa for 6 August 2014 at 0000 UTC from ERA5 reanalysis. The black star shows the location of Santiago city.

This day also shows a clear diurnal variation in the observed mean 2 m RH, 2 m temperature, and 10 m wind speed over the coastal and interior valleys (Figure 11a–f), which is similar to that shown in Figure 7 for the entire period of study. However, the near-surface wind speed does not show a clear diurnal variation this day at interior valley sites. Figure 5c,f show that, contrary to the near-surface temperature and RH, the wind speed over the study region is better simulated during unperturbed than during perturbed days (those affected by the passage of synoptic events). The diurnal variation was also considerably perturbed at mountain locations, with larger 2 m RH values, a cooler and nearly constant 2 m temperature, and a more intense and variable wind speed than that averaged over the entire period (Figure 11g–i). This is consistent with the system effecting earlier in the Andes foothills than in the valleys and coastal areas, misrepresenting the wind intensity and the system’s embedded circulations. Overall, lsm1 outperforms the other simulations representing the near-surface humidity and temperature, despite not being able to reproduce the minimum in relative humidity. The largest differences in the other simulations mainly occur during nighttime. On the other hand, the lsm3 simulation provides the best performance for 10 m wind speeds over coastal and valley areas.

The more intense precipitation (>5 mm) recorded by rain gauges on 6 August fell across a northwest–southeast band, and the largest values (>20 mm) were recorded to the east of Santiago city, in the Andes foothills (Figure 12a). Rainfall estimations from IMERG

also show the more intense precipitation along a northwest–southeast band over the domain (Figure 12b), and even show a region of relatively larger values in the Andes foothills, east/southeast of Santiago, as reported by the rain gauges. The WRF simulations largely overestimate the precipitation, mainly over the southern part of the domain (Figure 12c,d), although qualitatively they represent the region of maximum rainfall well. As described in Figure 9d–f, all simulations overestimate precipitation over the three sub-regions independently of the physics schemes employed. In addition, similar errors were present at coastal sites and interior valleys for the different rainfall thresholds, but they largely increased at mountain sites. Even though simulations are performed at a 1 km horizontal resolution, important regional orographic effects may be misrepresented in the model resulting in the described rainfall overestimation. The cu14 simulation, which shows the lowest RMSE and bias with observations over the whole domain and the entire period (Table 5), offers a much lower overestimation at the coastal and interior valley locations compared to no_ng (Table 7), which showed the worst agreement with observations.

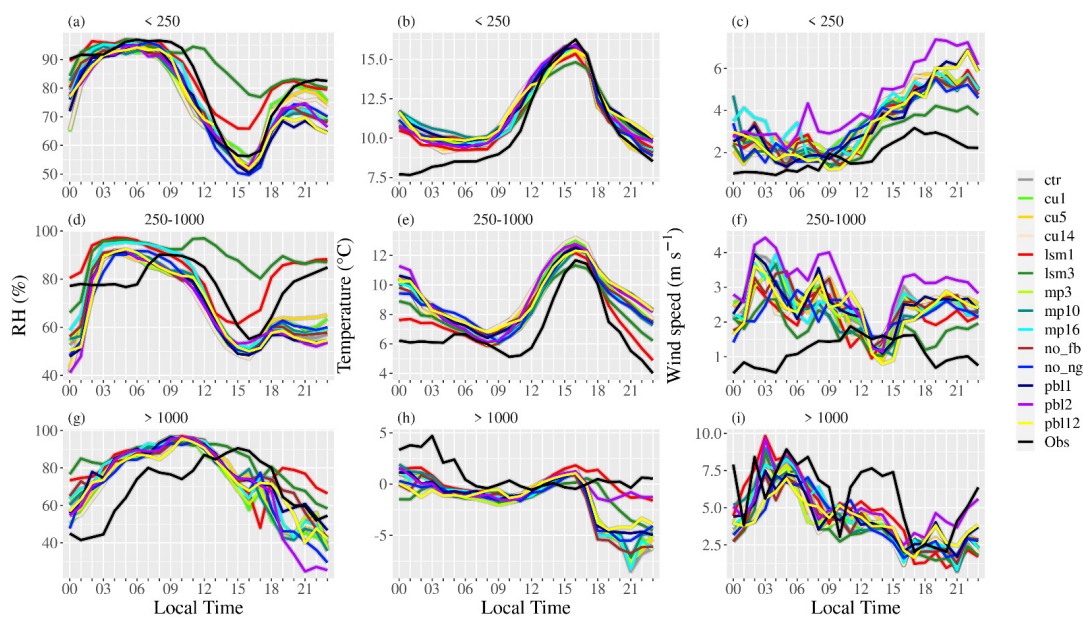


Figure 11. Diurnal variation of (a) 2 m RH, (b) 2 m temperature, and (c) 10 m wind speed from WRF simulations and observations for 6 August 2014, averaged over coastal stations. (d–f) and (g–i) same as (a–c), but for interior valleys and mountain locations, respectively.

Table 7. RMSE and bias of daily accumulated precipitation for cu14 and no_ng simulations over each sub-region for 6 August 2014 and 13 September 2014 study cases.

Day	Sim	RMSE			Bias		
		<250 m	250–1000 m	>1000 m	<250 m	250–1000 m	>1000 m
6 August 2014	cu14	13.9	8.9	10.5	10.8	6.2	9.3
6 August 2014	no_ng	17.5	11.4	11.2	14.6	9.2	9.8
13 September 2014	cu14	4.8	8.5	7.8	−2.5	−2.3	−0.6
13 September 2014	no_ng	5.2	8.7	11.8	−3.2	−5.2	2.9

Figure 13 shows the hourly evolution of precipitation from the observations and WRF simulations at Pirque station, which is located southeast of Santiago (33.6739° S, 70.58694° W and 663 m height), in the area where intense precipitation was reported on this day. All the simulations (except mp10, pbl12, and no_ng) predicted the starting time of precipitation at this site fairly well, but they overestimated the daily accumulated value and the duration of precipitation. The cu1, cu5, and cu14 simulations better represented

the evolution of precipitation at that site, highlighting that changing the cumulus schemes in the sensitivity experiments produced the largest improvement in precipitation forecasts in the region.

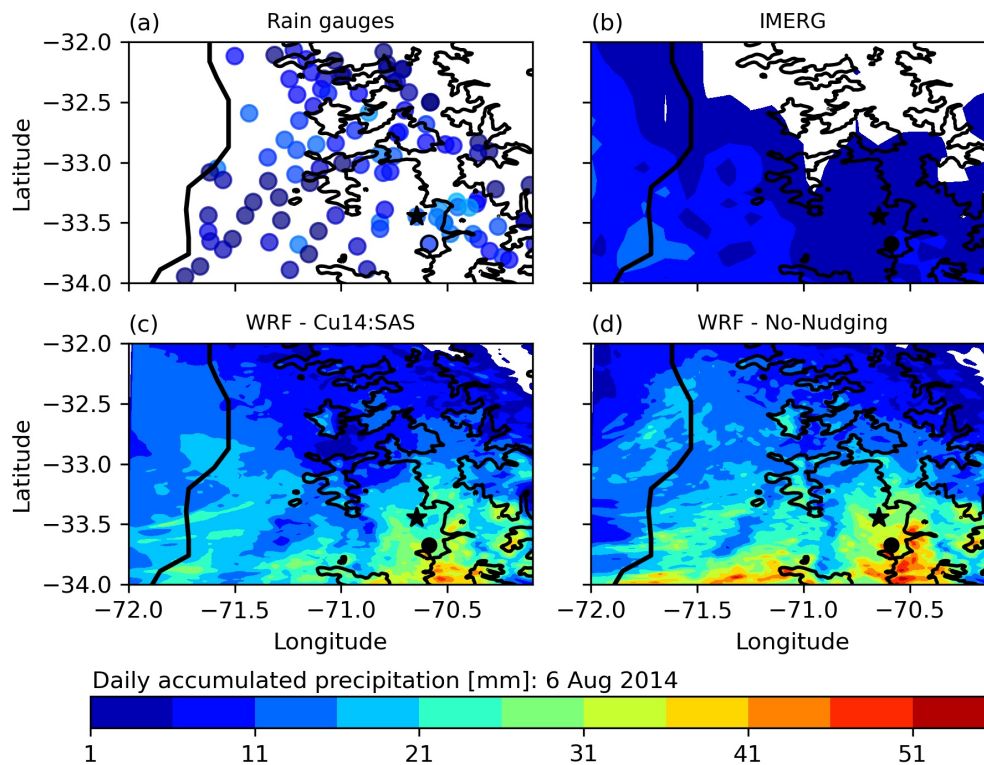


Figure 12. Horizontal distribution of daily accumulated precipitation (shaded color) from (a) rain gauges, (b) IMERG data, (c) WRF cu14 simulation, and (d) WRF no_ng simulation for 6 August 2014. The black solid lines represent the terrain height (intervals every 1 km, starting at 1 km). The black star and circle show the locations of DGA Santiago and Pirque rain gauges, respectively.

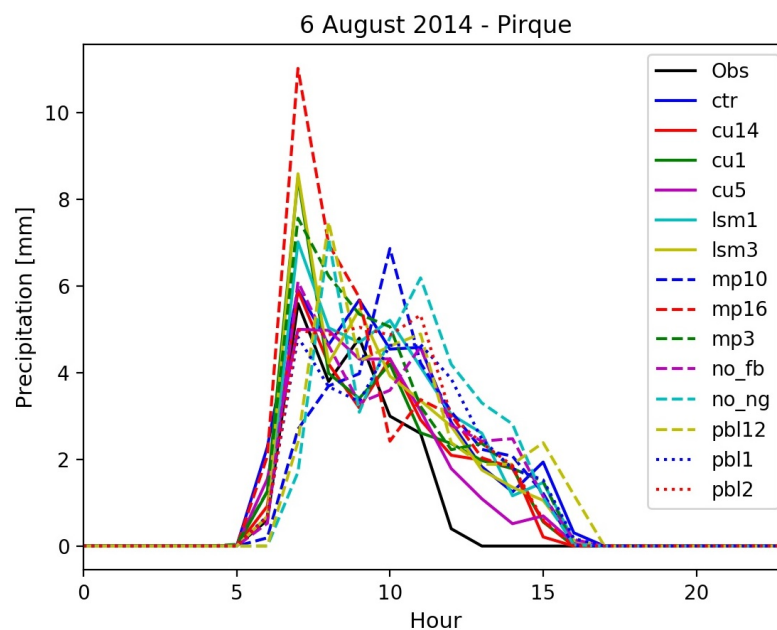


Figure 13. Hourly precipitation from rain gauges and WRF simulations at Pirque station (33.6739° S, 70.58694° W, and 663 m height).

3.3.2. Cut-Off Low: 13 September 2014

On 13 September 2014, a cut-off low developed offshore of the Chilean coast, showing its typical cold-core signature at mid-levels (Figure 14a) and an isolated lower pressure area at 300 hPa (Figure 14b). The system brought daily accumulated precipitation of less than 5 mm over most of the region, which started in the early morning. However, some stations in Santiago and in the foothills of the Andes reported daily accumulated precipitation between 10 and 20 mm.

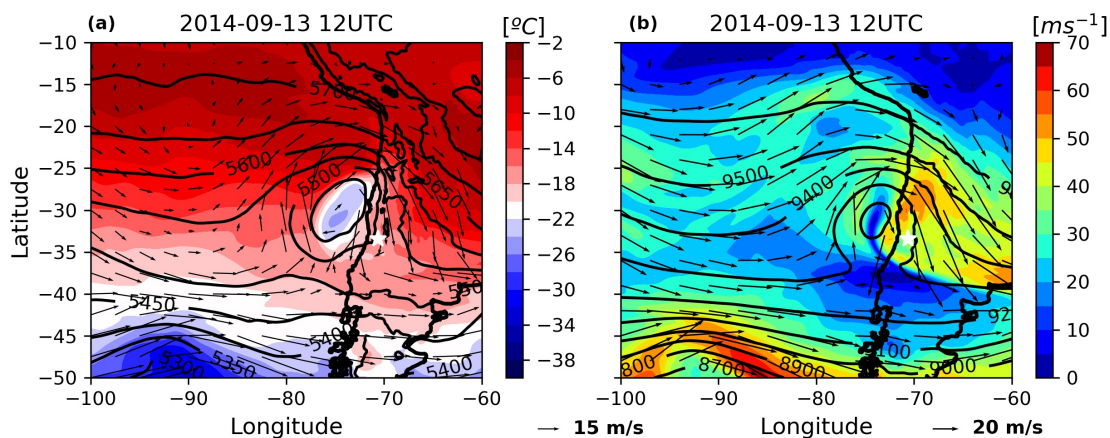


Figure 14. (a) The temperature (color shaded) and wind field at 500 hPa, and the 1000–500 hPa thickness (contours), and (b) the wind speed (color shaded), geopotential height (contours), and wind vectors at 300 hPa for 13 September 2014 at 1200 UTC from ERA5 reanalysis. The white star shows the location of Santiago city.

The cut-off low impacting this day did affect the observed mean near-surface temperature, humidity, and wind speed, averaged over the region of study, causing these variables to show a weakened or almost constant daily variation over coastal sites and interior valleys (Figure 15a–f). At mountain sites, the observed 2 m RH increased during the day to values larger than 90% (Figure 15g), the 2 m temperature steadily decreased (Figure 15h), and the 10 m wind speed was weak and highly variable (Figure 15i). The performance of the simulations was different in each of the sub-regions analyzed and the largest errors occurred over interior valleys and coastal locations. In general, the lsm1 (5-layer thermal LSM) simulation showed the best agreement with the observations representing the 2 m RH and 2 m temperature over coastal and interior valleys well, but not at mountain sites. All simulations overestimate the 10 m wind speed over coastal and valley areas, with the lsm3 (RUC LSM) showing the best agreement with the observations. At mountain sites, no simulations perform well, in part due to the largely variable nature of the near-surface wind on that day.

The most intense precipitation fell over higher altitudes in a northwest–southeast band along the foothills of the Andes (Figure 16a). The IMERG precipitation does not show a good agreement with the rain gauges this day (Figure 16b), although it shows larger precipitation values over the northeastern part of the domain, as was reported by the rain gauges. Although both WRF simulations (SAS scheme and no_ng) predicted reasonably well the spatial distribution of the most intense precipitation, they showed differences between them and with the observations (Figure 16c,d). The WRF SAS simulation predicted light precipitation at coastal locations, which increased inland and showed the most significant values over the Andes Cordillera in the eastern/northeastern part of the domain. However, it underestimated the precipitation over coastal locations and overestimated it over the Andes Cordillera. The no_ng simulation largely underestimated the precipitation over coastal locations and to the north of Santiago, whereas it largely overestimated the precipitation observed to the east of the Chilean capital.

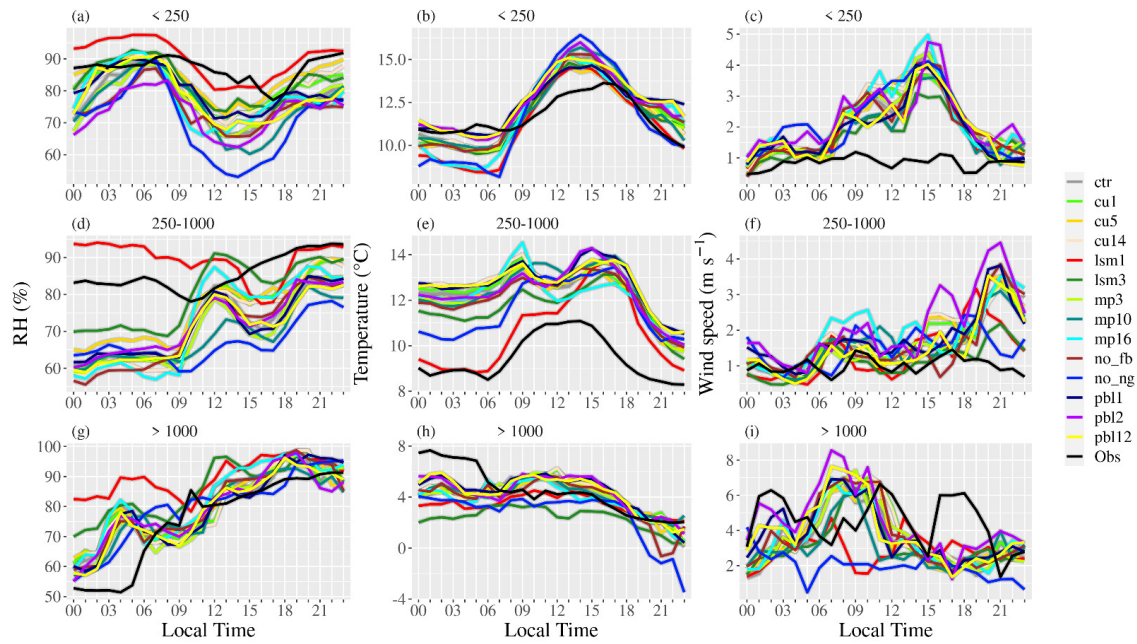


Figure 15. Same as Figure 11, but for 13 September 2014.

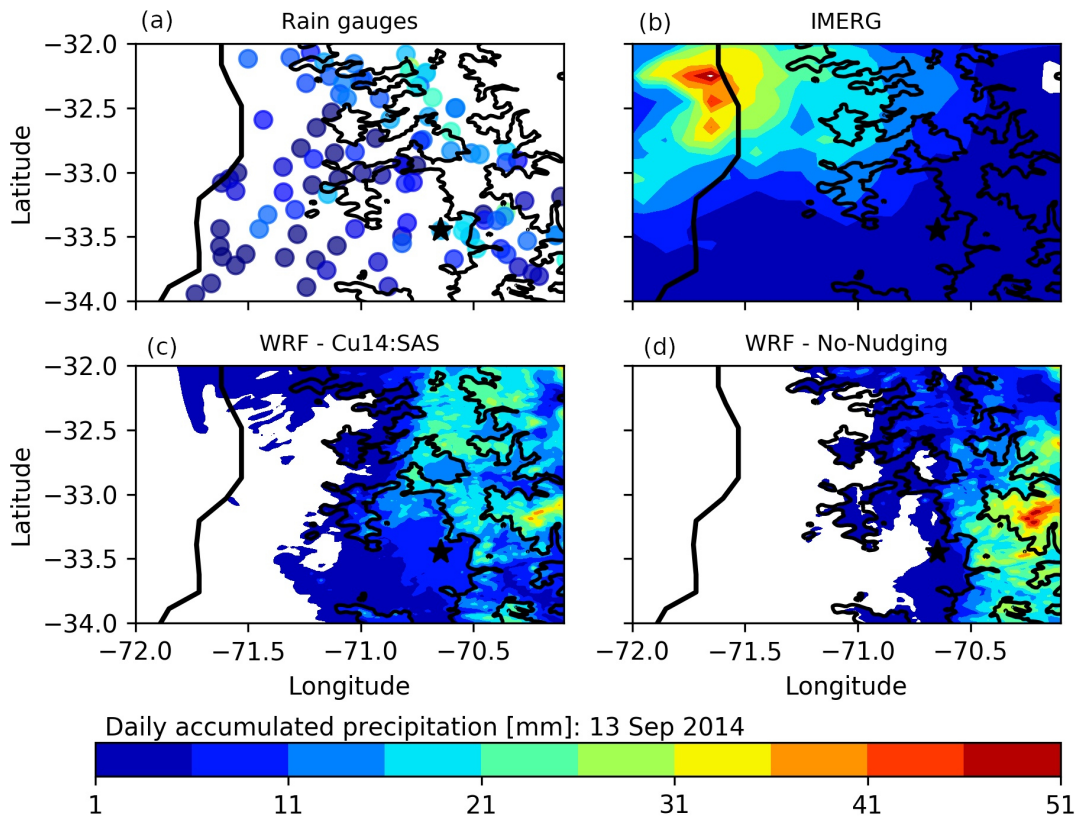


Figure 16. Horizontal distribution of daily accumulated precipitation (shaded color) from (a) rain gauges, (b) IMERG data, (c) WRF cu14 simulations, and (d) WRF no_ng simulation for 13 September 2014. The black solid lines represent the terrain height (intervals of 1 km, starting at 1 km). The black star shows the location of the DGA Santiago rain gauge.

4. Discussion and Conclusions

We conducted 14 high-resolution numerical sensitivity experiments with the WRF model over central Chile for 83 days during austral winter and spring (from 25 July to 15 October 2014). The complex terrain includes different geographical features (coastal, interior valleys, and mountain sites) that add difficulty in forecasting the atmospheric conditions over this region, where important economic sectors and almost half of the Chilean population reside. We tested several land-surface models, PBL, cumulus, and microphysics schemes, and we also evaluated using analysis nudging and two-way vs. one-way interactions among model domains. We assessed the physical schemes and parameters that showed the best and worst agreements with observations in the region as a whole but also focused on assessing the model performance over specific coastal, interior valleys, and mountain locations in central Chile.

The performance of the simulated 2 m temperature, 2 m RH, 10 m wind speed, and precipitation decreases in general from the coast to high-altitude sites. However, a slightly lower RMSE for wind speeds and better timing and representation of rain/no-rain events over interior valleys indicate that differences in wind speeds and precipitation between the coastal and interior valleys are not clear. This highlights the difficulty the model has in representing both the near-surface conditions and the precipitation enhancement over complex terrain. Similar results have been reported in other studies [35,36,64,65], although better agreements in near-surface temperature and humidity forecasts with observations at mountain rather than at coastal sites have also been found in WRF model studies [66].

Changing the LSM parameterization may cause the largest impact on 2 m RH, 2 m temperature, and 10 m wind speed forecasts in central Chile, whereas it does not significantly influence precipitation. The simulations using the 5-layer thermal diffusion (lsm1) and RUC (lsm3) LSM schemes show, in general, the best performance in simulating the 2 m temperature, 2 m RH, and the 10 m wind speed over coastal and interior valley locations. The lowest RMSE was found over coastal areas for 2 m temperature, 2 m RH, and 10 m wind speeds, 2.6 °C, 13.5%, and 1.6 ms⁻¹, respectively, whereas the lowest RMSEs obtained over interior valleys were 2.6 °C, 18.2%, and 1.2 ms⁻¹, respectively. Both simulations (lsm1 and lsm3) show a poor performance in representing the near-surface conditions over mountain sites. However, it is important to note that just a few stations were assessed over this area. Therefore, confidence in our results would increase if more mountain sites were available for our analysis. On the other hand, a controlled tuning of the LSM scheme could improve the representation of near-surface conditions in the WRF model, which is a topic of future research.

When forecasting the 10 m wind speed, the simulation using the RUC LSM shows the best performance in terms of absolute errors in coastal and interior valley locations. The statistical metrics for the simulation using the 5-layer thermal diffusion scheme are very close (the second-best compared to observations). Therefore, the 5-layer thermal diffusion LSM may be employed as an alternative to the RUC LSM scheme in studies focused on wind speed over central Chile. Contrary to our results, Ref. [21] reported that combining the RUC LSM with the MYYN PBL showed the worst performance in wind speed forecasts among a number of WRF sensitivity experiments over a region of complex terrain in Spain. However, its WRF configuration differed from ours in a number of other aspects, highlighting the difficulty in selecting a group of physical parameterizations that can successfully be used to accurately forecast different regions, atmospheric phenomena, and times of the year.

All the simulations represented a boundary layer warmer and drier than observed during the analyzed period. In contrast, they all simulated a cooler and moister free atmosphere. The largest errors in these variables occurred in the boundary layer (below 850 hPa) and they decreased with height. The simulations mainly overestimated the wind speed in the layer 1000–700 hPa, except in the transition region between the boundary layer and the free atmosphere, and a low-level jet was mainly simulated at lower heights than observed.

Changing the cumulus schemes produces the most significant improvement in precipitation forecasts by reducing the RMSE, the bias score (BS), and the false alarm ratio (FAR) over the region. However, the cumulus schemes show the lowest proportion of rainfall events that are successfully simulated by the model. The simplified Arakawa–Schubert (SAS) scheme showed the lowest RMSE (13.1 mm) and bias (3.7 mm). In addition, the cumulus choice does not seem to have significant impacts on the 2 m RH, 2 m temperature, and 10 m wind speeds. Ref. [67] showed that changing the cumulus parameterization in the WRF model causes the most considerable variations in convective development and precipitation compared to microphysics in the simulation of two case studies in the southern Great Plains.

Similar to what was found for the whole period of analysis, the simulations using the 5-layer thermal diffusion and the RUC LSM schemes better represented, in general, the near-surface variables during the days when a frontal system and a cut-off low impacted central Chile. On the other hand, the simulation using the SAS cumulus scheme also seemed to better represent precipitation when these two synoptic-scale events affected the region.

The results obtained in this study have shown which physical parameterization or parameter within the WRF model provides the best and the worst performance in the region for each specific variable analyzed. Although this allows us to identify the best WRF configuration for a specific research goal or the best operational model setting for the region, the assessment of these and other physical parameterizations over a much larger period of analysis (including other seasons) would be desirable in order to support the conclusions obtained in this study. In addition, other aspects, such as increasing the boundary condition update frequency or testing a different land-use database can be explored to improve the model performance in the region.

Author Contributions: Conceptualization, J.A., J.C.M. and G.R.; methodology, M.D., J.C.M. and J.A.; software, D.P.; validation, M.D., J.C.M. and J.A.; formal analysis, M.D. and J.C.M.; writing—original draft preparation, J.C.M. and J.A.; writing—review and editing, G.R., A.M.C. and D.B.; visualization, M.D. All authors have read and agreed to the published version of the manuscript.

Funding: This work was partially funded by ANID FONDEF ID22I10206.

Institutional Review Board Statement: Not applicable.

Informed Consent Statement: Not applicable.

Data Availability Statement: Precipitation data from several sources is gathered and provided from the Center for Climate Research and Resilience (CR2) through its website (<https://www.cr2.cl/datos-de-precipitacion/> (accessed on 15 July 2022)). The CR2 center also maintains the Vismet site (<http://vismet.cr2.cl/> (accessed on 15 July 2022)), which was used to visualize meteorological information for this study. The IMERG data were provided by the NASA/Goddard Space Flight Center and PPS, which develop and compute the IMERG data as a contribution to GPM, and archived at the NASA GES DISC., which is updated daily. NCEP Climate Forecast System Version 2 (CFSv2, [41]) provided 6-hourly data. Research Data Archive at the National Center for Atmospheric Research, Computational, and Information Systems Laboratory. <https://doi.org/10.5065/D61C1TXF>, accessed on 1 October 2020. The output from WRF simulations conducted in this study may be available to interested readers upon request.

Acknowledgments: J.C.M. and D.P. acknowledge the Interdisciplinary Center of Atmospheric and Astro-Statistical Studies at Universidad de Valparaíso. This work was partially supported by ANID FONDEF ID22I10206. Powered@NLHPC: This research was partially supported by the supercomputing infrastructure of the National Laboratory for High Performing Computer (NLHPC) (ECM-02).

Conflicts of Interest: The authors declare no conflict of interest.

References

1. Di Castri, F.; Hajek, E.R. *Bioclimatología de Chile*; Vicerrectoría Académica de la Universidad Católica de Chile Santiago: Santiago, Chile, 1976; Volume 128.
2. Miller, J. The climate of Chile. In *Climates of Central and South America*; Schwerdtfeger, W., Ed.; Elsevier Scientific Publishing Company: New York, NY, USA, 1976.
3. Rodwell, M.J.; Hoskins, B.J. Subtropical anticyclones and summer monsoons. *J. Clim.* **2001**, *14*, 3192–3211. [[CrossRef](#)]
4. Barrett, B.S.; Hameed, S. Seasonal variability in precipitation in central and southern Chile: Modulation by the South Pacific high. *J. Clim.* **2017**, *30*, 55–69. [[CrossRef](#)]
5. Pizarro, J.; Montecinos, A. Cutoff cyclones off the subtropical coast of Chile. In Proceedings of the Sixth International Conference on Southern Hemisphere Meteorology and Oceanography, Santiago, Chile, 3–7 April 2000; pp. 278–279.
6. Fuenzalida, H.A.; Sánchez, R.; Garreaud, R.D. A climatology of cutoff lows in the Southern Hemisphere. *J. Geophys. Res. Atmos.* **2005**, *110*, D18101. [[CrossRef](#)]
7. Reboita, M.S.; Nieto, R.; Gimeno, L.; Da Rocha, R.P.; Ambrizzi, T.; Garreaud, R.; Krüger, L.F. Climatological features of cutoff low systems in the Southern Hemisphere. *J. Geophys. Res. Atmos.* **2010**, *115*, D17104. [[CrossRef](#)]
8. Bozkurt, D.; Rondanelli, R.; Garreaud, R.; Arriagada, A. Impact of warmer eastern tropical Pacific SST on the March 2015 Atacama floods. *Mon. Weather. Rev.* **2016**, *144*, 4441–4460. [[CrossRef](#)]
9. Bretherton, C.S.; Uttal, T.; Fairall, C.W.; Yuter, S.E.; Weller, R.A.; Baumgardner, D.; Comstock, K.; Wood, R.; Raga, G.B. The EPIC 2001 stratocumulus study. *Bull. Am. Meteorol. Soc.* **2004**, *85*, 967–978. [[CrossRef](#)]
10. Comstock, K.K.; Bretherton, C.S.; Yuter, S.E. Mesoscale variability and drizzle in southeast Pacific stratocumulus. *J. Atmos. Sci.* **2005**, *62*, 3792–3807. [[CrossRef](#)]
11. Hannay, C.; Williamson, D.L.; Hack, J.J.; Kiehl, J.T.; Olson, J.G.; Klein, S.A.; Bretherton, C.S.; Köhler, M. Evaluation of forecasted southeast Pacific stratocumulus in the NCAR, GFDL, and ECMWF models. *J. Clim.* **2009**, *22*, 2871–2889. [[CrossRef](#)]
12. Muñoz, R.C.; Undurraga, A.A. Daytime mixed layer over the Santiago Basin: Description of two years of observations with a lidar ceilometer. *J. Appl. Meteorol. Climatol.* **2010**, *49*, 1728–1741. [[CrossRef](#)]
13. Garreaud, R.; Rutllant, J.; Fuenzalida, H. Coastal lows along the subtropical west coast of South America: Mean structure and evolution. *Mon. Weather. Rev.* **2002**, *130*, 75–88. [[CrossRef](#)]
14. Bauer, P.; Thorpe, A.; Brunet, G. The quiet revolution of numerical weather prediction. *Nature* **2015**, *525*, 47–55. [[CrossRef](#)] [[PubMed](#)]
15. Rotach, M.W.; Stiperski, I.; Fuhrer, O.; Goger, B.; Gohm, A.; Obleitner, F.; Rau, G.; Sfyri, E.; Vergeiner, J. Investigating exchange processes over complex topography: The Innsbruck box (i-Box). *Bull. Am. Meteorol. Soc.* **2017**, *98*, 787–805. [[CrossRef](#)]
16. Jankov, I.; Bao, J.W.; Neiman, P.J.; Schultz, P.J.; Yuan, H.; White, A.B. Evaluation and comparison of microphysical algorithms in ARW-WRF model simulations of atmospheric river events affecting the California coast. *J. Hydrometeorol.* **2009**, *10*, 847–870. [[CrossRef](#)]
17. Ruiz, J.J.; Saulo, C.; Nogués-Paegle, J. WRF model sensitivity to choice of parameterization over South America: Validation against surface variables. *Mon. Weather. Rev.* **2010**, *138*, 3342–3355. [[CrossRef](#)]
18. Carvalho, D.; Rocha, A.; Gómez-Gesteira, M.; Santos, C.S. Sensitivity of the WRF model wind simulation and wind energy production estimates to planetary boundary layer parameterizations for onshore and offshore areas in the Iberian Peninsula. *Appl. Energy* **2014**, *135*, 234–246. [[CrossRef](#)]
19. Gómez-Navarro, J.J.; Raible, C.C.; Dierer, S. Sensitivity of the WRF model to PBL parametrizations and nesting techniques: Evaluation of wind storms over complex terrain. *Geosci. Model Dev.* **2015**, *8*, 3349–3363. [[CrossRef](#)]
20. Orr, A.; Listowski, C.; Couttet, M.; Collier, E.; Immerzeel, W.; Deb, P.; Bannister, D. Sensitivity of simulated summer monsoonal precipitation in Langtang Valley, Himalaya, to cloud microphysics schemes in WRF. *J. Geophys. Res. Atmos.* **2017**, *122*, 6298–6318. [[CrossRef](#)]
21. Fernández-González, S.; Martín, M.L.; García-Ortega, E.; Merino, A.; Lorenzana, J.; Sánchez, J.L.; Valero, F.; Rodrigo, J.S. Sensitivity analysis of the WRF model: Wind-resource assessment for complex terrain. *J. Appl. Meteorol. Climatol.* **2018**, *57*, 733–753. [[CrossRef](#)]
22. Posada-Marín, J.A.; Rendón, A.M.; Salazar, J.F.; Mejía, J.F.; Villegas, J.C. WRF downscaling improves ERA-Interim representation of precipitation around a tropical Andean valley during El Niño: Implications for GCM-scale simulation of precipitation over complex terrain. *Clim. Dyn.* **2019**, *52*, 3609–3629. [[CrossRef](#)]
23. Falasca, S.; Gandolfi, I.; Argentini, S.; Barnaba, F.; Casasanta, G.; Di Liberto, L.; Petenko, I.; Curci, G. Sensitivity of near-surface meteorology to PBL schemes in WRF simulations in a port-industrial area with complex terrain. *Atmos. Res.* **2021**, *264*, 105824. [[CrossRef](#)]
24. Aravind, A.; Srinivas, C.; Shrivastava, R.; Hegde, M.; Seshadri, H.; Mohapatra, D. Simulation of atmospheric flow field over the complex terrain of Kaiga using WRF: Sensitivity to model resolution and PBL physics. *Meteorol. Atmos. Phys.* **2022**, *134*, 1–25. [[CrossRef](#)]
25. Moya-Álvarez, A.S.; Martínez-Castro, D.; Kumar, S.; Estevan, R.; Silva, Y. Response of the WRF model to different resolutions in the rainfall forecast over the complex Peruvian orography. *Theor. Appl. Climatol.* **2019**, *137*, 2993–3007. [[CrossRef](#)]

26. Moya-Alvarez, A.S.; Martínez-Castro, D.; Flores, J.L.; Silva, Y. Sensitivity study on the influence of parameterization schemes in WRF_ARW model on short-and medium-range precipitation forecasts in the Central Andes of Peru. *Adv. Meteorol.* **2018**, *2018*, 1381092. [[CrossRef](#)]
27. Martínez-Castro, D.; Kumar, S.; Flores Rojas, J.L.; Moya-Álvarez, A.; Valdivia-Prado, J.M.; Villalobos-Puma, E.; Castillo-Velarde, C.D.; Silva-Vidal, Y. The impact of microphysics parameterization in the simulation of two convective rainfall events over the central Andes of Peru using WRF-ARW. *Atmosphere* **2019**, *10*, 442. [[CrossRef](#)]
28. Yáñez-Morrón, G.; Gironás, J.; Caneo, M.; Delgado, R.; Garreaud, R. Using the Weather Research and Forecasting (WRF) model for precipitation forecasting in an Andean region with complex topography. *Atmosphere* **2018**, *9*, 304. [[CrossRef](#)]
29. Marín, J.C.; Pozo, D.; Mlawer, E.; Turner, D.D.; Curé, M. Dynamics of local circulations in mountainous terrain during the RHUBC-II project. *Mon. Weather. Rev.* **2013**, *141*, 3641–3656. [[CrossRef](#)]
30. Fonseca, R.; Zorzano-Mier, M.P.; Azua-Bustos, A.; González-Silva, C.; Martín-Torres, J. A surface temperature and moisture intercomparison study of the Weather Research and Forecasting model, in-situ measurements and satellite observations over the Atacama Desert. *Q. J. R. Meteorol. Soc.* **2019**, *145*, 2202–2220. [[CrossRef](#)]
31. Muñoz, R.C.; Falvey, M.J.; Arancibia, M.; Astudillo, V.I.; Elgueta, J.; Ibarra, M.; Santana, C.; Vásquez, C. Wind energy exploration over the Atacama desert: A numerical model–guided observational program. *Bull. Am. Meteorol. Soc.* **2018**, *99*, 2079–2092. [[CrossRef](#)]
32. de Linaje, N.G.A.; Mattar, C.; Borvarán, D. Quantifying the wind energy potential differences using different WRF initial conditions on Mediterranean coast of Chile. *Energy* **2019**, *188*, 116027. [[CrossRef](#)]
33. Salfate, I.; Marín, J.C.; Cuevas, O.; Montecinos, S. Improving wind speed forecasts from the Weather Research and Forecasting model at a wind farm in the semiarid Coquimbo region in central Chile. *Wind. Energy* **2020**, *23*, 1939–1954. [[CrossRef](#)]
34. Jiménez, P.; García-Bustamante, E.; González-Rouco, J.; Valero, F.; Montávez, J.; Navarro, J. Surface wind regionalization in complex terrain. *J. Appl. Meteorol. Climatol.* **2008**, *47*, 308–325. [[CrossRef](#)]
35. Jiménez, P.A.; González-Rouco, J.F.; García-Bustamante, E.; Navarro, J.; Montávez, J.P.; De Arellano, J.V.G.; Dudhia, J.; Muñoz-Roldan, A. Surface wind regionalization over complex terrain: Evaluation and analysis of a high-resolution WRF simulation. *J. Appl. Meteorol. Climatol.* **2010**, *49*, 268–287. [[CrossRef](#)]
36. Jiménez, P.A.; Dudhia, J. On the ability of the WRF model to reproduce the surface wind direction over complex terrain. *J. Appl. Meteorol. Climatol.* **2013**, *52*, 1610–1617. [[CrossRef](#)]
37. Skamarock, W.C.; Klemp, J.B.; Dudhia, J.; Gill, D.O.; Barker, D.M.; Duda, M.G.; Huang, X.Y.; Wang, W.; Powers, J.G. A description of the advanced research WRF version 3. *NCAR Tech. Note* **2008**, *475*, 113.
38. Marín, J.C.; Raga, G.B.; Arévalo, J.; Baumgardner, D.; Córdova, A.M.; Pozo, D.; Calvo, A.; Castro, A.; Fraile, R.; Sorribas, M. Properties of particulate pollution in the port city of Valparaíso, Chile. *Atmos. Environ.* **2017**, *171*, 301–316. [[CrossRef](#)]
39. Pozo, D.; Marín, J.C.; Raga, G.B.; Arévalo, J.; Baumgardner, D.; Córdova, A.M.; Mora, J. Synoptic and local circulations associated with events of high particulate pollution in Valparaíso, Chile. *Atmos. Environ.* **2019**, *196*, 164–178. [[CrossRef](#)]
40. Cordova, A.M.; Arévalo, J.; Marín, J.C.; Baumgardner, D.; Raga, G.B.; Pozo, D.; Ochoa, C.A.; Rondanelli Rojas, R. On the transport of urban pollution in an Andean mountain valley. *Aerosol Air Qual. Res.* **2016**, *16*, 593–605. [[CrossRef](#)]
41. Saha, S.; Moorthi, S.; Wu, X.; Wang, J.; Nadiga, S.; Tripp, P.; Behringer, D.; Hou, Y.T.; Chuang, H.Y.; Iredell, M.; et al. The NCEP climate forecast system version 2. *J. Clim.* **2014**, *27*, 2185–2208. [[CrossRef](#)]
42. Deng, A.; Stauffer, D.R.; Dudhia, J.; Otte, T.; Hunter, G.K. Update on analysis nudging FDDA in WRF-ARW. In Proceedings of the 8th WRF Users' Workshop, Boulder, CO, USA, 11–15 June 2007; p. 35.
43. Bowden, J.H.; Otte, T.L.; Nolte, C.G.; Otte, M.J. Examining interior grid nudging techniques using two-way nesting in the WRF model for regional climate modeling. *J. Clim.* **2012**, *25*, 2805–2823. [[CrossRef](#)]
44. Bowden, J.H.; Nolte, C.G.; Otte, T.L. Simulating the impact of the large-scale circulation on the 2-m temperature and precipitation climatology. *Clim. Dyn.* **2013**, *40*, 1903–1920. [[CrossRef](#)]
45. Mlawer, E.J.; Taubman, S.J.; Brown, P.D.; Iacono, M.J.; Clough, S.A. Radiative transfer for inhomogeneous atmospheres: RRTM, a validated correlated-k model for the longwave. *J. Geophys. Res. Atmos.* **1997**, *102*, 16663–16682. [[CrossRef](#)]
46. Tiedtke, M. A comprehensive mass flux scheme for cumulus parameterization in large-scale models. *Mon. Weather. Rev.* **1989**, *117*, 1779–1800. [[CrossRef](#)]
47. Zhang, C.; Wang, Y.; Hamilton, K. Improved representation of boundary layer clouds over the southeast Pacific in ARW-WRF using a modified Tiedtke cumulus parameterization scheme. *Mon. Weather. Rev.* **2011**, *139*, 3489–3513. [[CrossRef](#)]
48. Hong, S.Y.; Noh, Y.; Dudhia, J. A new vertical diffusion package with an explicit treatment of entrainment processes. *Mon. Weather. Rev.* **2006**, *134*, 2318–2341. [[CrossRef](#)]
49. Nakanishi, M.; Niino, H. An improved Mellor–Yamada level-3 model: Its numerical stability and application to a regional prediction of advection fog. *Bound.-Layer Meteorol.* **2006**, *119*, 397–407. [[CrossRef](#)]
50. Chen, F.; Dudhia, J. Coupling an advanced land surface–hydrology model with the Penn State–NCAR MM5 modeling system. Part I: Model implementation and sensitivity. *Mon. Weather. Rev.* **2001**, *129*, 569–585. [[CrossRef](#)]
51. Dudhia, J. A multi-layer soil temperature model for MM5. In Proceedings of the Preprints, The Sixth PSU/NCAR Mesoscale Model Users' Workshop, Boulder CO, USA, 22–24 July 1996; pp. 22–24.
52. Benjamin, S.G.; Grell, G.A.; Brown, J.M.; Smirnova, T.G.; Bleck, R. Mesoscale weather prediction with the RUC hybrid isentropic–terrain-following coordinate model. *Mon. Weather. Rev.* **2004**, *132*, 473–494. [[CrossRef](#)]

53. Janjić, Z.I. The step-mountain eta coordinate model: Further developments of the convection, viscous sublayer, and turbulence closure schemes. *Mon. Weather. Rev.* **1994**, *122*, 927–945. [[CrossRef](#)]
54. Grenier, H.; Bretherton, C.S. A moist PBL parameterization for large-scale models and its application to subtropical cloud-topped marine boundary layers. *Mon. Weather. Rev.* **2001**, *129*, 357–377. [[CrossRef](#)]
55. Kain, J.S. The Kain–Fritsch convective parameterization: An update. *J. Appl. Meteorol.* **2004**, *43*, 170–181. [[CrossRef](#)]
56. Grell, G.A. Prognostic evaluation of assumptions used by cumulus parameterizations. *Mon. Weather. Rev.* **1993**, *121*, 764–787. [[CrossRef](#)]
57. Grell, G.A.; Dévényi, D. A generalized approach to parameterizing convection combining ensemble and data assimilation techniques. *Geophys. Res. Lett.* **2002**, *29*, 38-1–38-4. [[CrossRef](#)]
58. Han, J.; Pan, H.L. Revision of convection and vertical diffusion schemes in the NCEP Global Forecast System. *Weather. Forecast.* **2011**, *26*, 520–533. [[CrossRef](#)]
59. Hong, S.Y.; Dudhia, J.; Chen, S.H. A revised approach to ice microphysical processes for the bulk parameterization of clouds and precipitation. *Mon. Weather. Rev.* **2004**, *132*, 103–120. [[CrossRef](#)]
60. Morrison, H.; Thompson, G.; Tatarskii, V. Impact of cloud microphysics on the development of trailing stratiform precipitation in a simulated squall line: Comparison of one-and two-moment schemes. *Mon. Weather. Rev.* **2009**, *137*, 991–1007. [[CrossRef](#)]
61. Lim, K.S.S.; Hong, S.Y. Development of an effective double-moment cloud microphysics scheme with prognostic cloud condensation nuclei (CCN) for weather and climate models. *Mon. Weather. Rev.* **2010**, *138*, 1587–1612. [[CrossRef](#)]
62. Bullock Jr, O.R.; Alapaty, K.; Herwehe, J.A.; Mallard, M.S.; Otte, T.L.; Gilliam, R.C.; Nolte, C.G. An observation-based investigation of nudging in WRF for downscaling surface climate information to 12-km grid spacing. *J. Appl. Meteorol. Climatol.* **2014**, *53*, 20–33. [[CrossRef](#)]
63. Wootten, A.; Bowden, J.; Boyles, R.; Terando, A. The sensitivity of WRF downscaled precipitation in Puerto Rico to cumulus parameterization and interior grid nudging. *J. Appl. Meteorol. Climatol.* **2016**, *55*, 2263–2281. [[CrossRef](#)]
64. Zhang, H.; Pu, Z.; Zhang, X. Examination of errors in near-surface temperature and wind from WRF numerical simulations in regions of complex terrain. *Weather. Forecast.* **2013**, *28*, 893–914. [[CrossRef](#)]
65. Kantha Rao, B.; Rakesh, V. Evaluation of WRF-simulated multilevel soil moisture, 2-m air temperature, and 2-m relative humidity against in situ observations in India. *Pure Appl. Geophys.* **2019**, *176*, 1807–1826. [[CrossRef](#)]
66. Lu, W.; Zhong, S.; Charney, J.; Bian, X.; Liu, S. WRF simulation over complex terrain during a southern California wildfire event. *J. Geophys. Res. Atmos.* **2012**, *117*. [[CrossRef](#)]
67. Jeworrek, J.; West, G.; Stull, R. Evaluation of cumulus and microphysics parameterizations in WRF across the convective gray zone. *Weather. Forecast.* **2019**, *34*, 1097–1115. [[CrossRef](#)]

Disclaimer/Publisher’s Note: The statements, opinions and data contained in all publications are solely those of the individual author(s) and contributor(s) and not of MDPI and/or the editor(s). MDPI and/or the editor(s) disclaim responsibility for any injury to people or property resulting from any ideas, methods, instructions or products referred to in the content.